



# Characterization of aerosol Stokes number in 90° bends and idealized extrathoracic airways



L. Nicolaou<sup>a</sup>, T.A. Zaki<sup>b</sup>

<sup>a</sup> Department of Mechanical Engineering, Imperial College London, Exhibition Road, London SW7 2AZ, UK

<sup>b</sup> Department of Mechanical Engineering, Johns Hopkins University, Baltimore, MD21218, USA

## ARTICLE INFO

### Keywords:

Particle deposition  
Stokes number  
Curved pipe  
Respiratory airways  
Direct numerical simulation (DNS)

## ABSTRACT

Prediction of aerosol deposition in the respiratory system is important for improving the efficiency of inhaled drug delivery and for assessing the toxicity of airborne pollutants. Deposition is typically reported as a function of a global Stokes number which is based on a reference flow timescale, or the ratio of the characteristic flow length and velocity scales. In reality, however, particles experience varying flow timescales as they are advected through the airways, which motivates the use of an instantaneous Stokes number based on the local properties of the flow field. We then define the effective Stokes number as the time-average of the instantaneous value. This effective Stokes number thus encapsulates the flow history and geometric variability, and provides a more detailed account of the particle trajectory in the flow. Laminar and turbulent flows in a curved pipe are examined first and provide a simplified, or canonical, configuration of the flow in the upper airways. They are followed by a study of turbulent flow in an idealized mouth–throat geometry. Our results demonstrate that the effective Stokes number can deviate significantly from the traditional value based solely on the reference flow timescale. In addition, the effective Stokes number shows a clear correlation with deposition efficiency and can therefore be used to determine optimal aerosol release locations in order to minimize extrathoracic losses.

## 1. Introduction

Inhaled drug delivery is the main form of treatment for a number of respiratory diseases, such as asthma and chronic obstructive pulmonary disease (COPD). Knowledge of the aerosol deposition in the extrathoracic, or upper, airways is critical in the design of effective inhalation devices for optimum delivery to the lungs. The deposition is, however, highly dependent on the flow regime. In the upper airways, where the flow is turbulent or transitional, deposition occurs primarily via impaction as well as turbulent dispersion for the smaller particles. As the airways become smaller and the air velocity decreases, the flow laminarizes and deposition tends to occur due to sedimentation. For submicron particles in the small airways, Brownian diffusion becomes the dominant mechanism. The flow dynamics also vary significantly across subjects due to geometric variation of the airways, thereby resulting in large deviation in the deposition patterns and efficiencies (Grgic, Finlay, Burnell, & Heenan, 2004; Nicolaou & Zaki, 2013; Stahlhofen, Gebhart, & Heyder, 1981).

For efficient drug delivery to the target areas in the lung, the inhaled aerosol must first clear the mouth and throat. Often, however, large aerosol losses occur in this region. Therefore, in the optimization of inhaled drug delivery, many studies have focused

E-mail addresses: [laura.nicolaou@imperial.ac.uk](mailto:laura.nicolaou@imperial.ac.uk) (L. Nicolaou), [t.zaki@jhu.edu](mailto:t.zaki@jhu.edu) (T.A. Zaki).

<http://dx.doi.org/10.1016/j.jaerosci.2016.09.003>

Received 11 May 2016; Received in revised form 3 August 2016; Accepted 21 September 2016

Available online 25 September 2016

0021-8502/ © 2016 Elsevier Ltd. All rights reserved.

on understanding and minimizing extrathoracic deposition. A number of *in vitro* experiments have examined the effects of particle size and flow rate on deposition in the mouth and throat (Cheng, Zhou, & Chen, 1999; Grgic, Finlay, & Heenan, 2004), as well as the effect of geometric variation (Grgic, Finlay, Burnell, et al., 2004; Heenan, Finlay, Grgic, Pollard, & Burnell, 2004). Advances in computing and numerical modelling techniques in the last decade have enabled increasingly more accurate simulations of the flow (Ball, Uddin, & Pollard, 2008; Heenan, Matida, Pollard, & Finlay, 2003; Lin, Tawhai, McLennan, & Hoffman, 2007; Nicolaou & Zaki, 2013) and aerosol deposition in the airways (Debhi, 2011; Jayaraju, Brouns, Verbanck, & Lacor, 2007; Kleinstreuer & Zhang, 2003; Li, Kleinstreuer, & Zhang, 2007; Matida, Finlay, Lange, & Grgic, 2004). The simulations can provide a detailed representation of the flow and the particle trajectories, compared to *in vitro* and *in vivo* studies. However, accurate and efficient prediction of the deposition remains challenging, due to the complexity of the airway geometries and of the flow. For this reason, many of the numerical studies on extrathoracic deposition have focused primarily on examining the suitability of various turbulence models and particle-tracking schemes (Debhi, 2011; Jayaraju et al., 2008; Matida et al., 2004; Stapleton et al., 2000).

Aerosols produced by inhalation devices are dilute dispersed flows which can be modelled using an Eulerian or a Lagrangian approach. The Eulerian, or two-fluid, approach treats the dispersed phase as a continuum, solving the conservation equations of particle mass and momentum. On the other hand, the Lagrangian approach treats the dispersed phase as a set of individual point-particles in a continuous carrier phase. The particles are tracked through the flow field by solving the equations of motion for each particle with the relevant forces acting on it. Description of turbulent dispersion and collision of particles with the airway walls is more natural with this approach. For this reason, the Lagrangian approach has featured prominently in studies of aerosol deposition in the airways (Debhi, 2011; Jayaraju et al., 2007; Kleinstreuer & Zhang, 2003; Li et al., 2007; Matida et al., 2004).

In order to characterize deposition in the extrathoracic airways a ‘lumped’ reference Stokes number, which is based on the mean diameter and mean flow velocity, is typically adopted in the literature. The deposition efficiency versus reference Stokes number, which follows an ‘S’ curve (Cheng et al., 1999; Grgic, Finlay, Burnell, et al., 2004), and deposition patterns for different particle sizes have been examined (Grgic, Finlay, Burnell, et al., 2004; Jayaraju et al., 2007; Zhang et al., 2002). Scatter in the deposition data can be observed when plotted against Stokes number, and is often attributed to the qualitative differences in the flow at different flow rates, and across subjects as a result of geometric variation. *In vitro* experiments performed by Grgic, Finlay, and Heenan (2004) in an idealized mouth–throat geometry showed that results at different flow rates appeared to lie on different curves, indicating a possible dependence on the Reynolds number. An empirical Reynolds number correction,  $Re^{0.37}$ , was applied to the Stokes number, collapsing their data onto one curve. Examination of the flow fields in a number of realistic mouth–throat geometries allowed Nicolaou and Zaki (2013) to explain the physical significance of this Reynolds number correction, which was attributed to at least two contributing factors: (1) the qualitative difference in the mean flow characteristics and (2) the difference in turbulence intensity. Using the viscous particle relaxation time,  $\tau_p^+$ , they provided an explanation of the Reynolds number dependence.

The reference Stokes number, and even the Reynolds number correction, do not take into account the varying flow timescales that particles experience as they are advected through the flow. In order to better characterize the particle transport and deposition we therefore propose the use of an instantaneous Stokes number based on the local flow properties. We subsequently define the particle’s effective Stokes number as the time-average of the instantaneous value. This effective Stokes number thus encapsulates the flow history and geometric variability, and is more representative of the particle trajectories. Laminar and turbulent flow cases in a curved pipe are considered first, followed by turbulent flow in an idealized mouth–throat geometry. In all cases, direct numerical simulations are performed and a Lagrangian–Eulerian approach is adopted for computing the particle trajectories.

The paper is organized as follows: In Section 2, the numerical method adopted for the solution of the flow equations and the particle tracking is described in detail, and the definitions of the instantaneous and effective Stokes numbers are introduced. In Section 3, results are presented for laminar and turbulent flow in a bent pipe, and for turbulent flow in an idealized mouth–throat geometry. Finally, Section 4 is a summary of the work and main findings.

## 2. Numerical method

### 2.1. Flow field

The Navier–Stokes equations are solved using a finite volume formulation, following the method by Rosenfeld, Kwak, and Vinokur (1991). Time integration is performed via a second-order semi-implicit fractional step method that uses Crank–Nicolson for the diffusive terms and Adams–Bashforth for the convective terms. The pressure Poisson equation is solved using a multi-grid algorithm with line-relaxation. Parallelism is achieved using message-passing interface (MPI). The algorithm has been adopted in a number of studies of transitional flows where accurately capturing the growth of flow instabilities is a primary consideration (Jung & Zaki, 2015; Zaki, 2013) and in direct numerical simulations of fully-turbulent flows where all the flow scales must be resolved (Jelly, Jung, & Zaki, 2014; Lee, Jung, Sung, & Zaki, 2013). Here too we perform direct numerical simulations which resolve all the flow scales, and therefore no turbulence modelling is necessary.

In order to model the complex airway geometries, a direct-forcing immersed boundary (IB) method developed for curvilinear grids is adopted (Nicolaou, Jung, & Zaki, 2015). The no-slip boundary condition at the airway walls is enforced via a momentum forcing term and mass conservation is satisfied via a mass source term in cells containing the immersed boundary. The discretized equations are given by

$$\frac{\hat{\mathbf{u}} - \mathbf{u}^{n-1}}{\Delta t} = -\left(\frac{1}{2}N(\mathbf{u}^{n-1}) + \frac{1}{2}N(\mathbf{u}^{n-2})\right) - \nabla p^{n-1} + \frac{1}{Re}\left(\frac{3}{2}L(\hat{\mathbf{u}}) - \frac{1}{2}L(\mathbf{u}^{n-1})\right) + \mathbf{f}^n \quad (1)$$

$$\nabla^2 \phi^n = \frac{1}{\Delta t} (\nabla \cdot \hat{\mathbf{u}} - q^n) \quad (2)$$

$$\mathbf{u}^n = \hat{\mathbf{u}} - \Delta t \nabla \phi^n \quad (3)$$

$$p^n = p^{n-1} + \phi^n \quad (4)$$

where  $\mathbf{f}$  is the momentum forcing vector added on the boundary and outside the fluid in order to satisfy no-slip at the immersed boundary,  $q$  is the mass source/sink applied to cells containing the immersed boundary in order to ensure mass conservation,  $N(\mathbf{u})$  are the convective terms and  $L(\mathbf{u})$  are the implicit diffusive terms.

The main advantage of the IB approach is that it allows the use of relatively simple structured grids to model complex geometries, such as the respiratory airways. We herein adopt a curvilinear implementation of the IB method. Use of a curvilinear grid, rather than the commonly used Cartesian grids, improves computational efficiency by minimizing the number of grid points outside the fluid domain (see Figs. 1 and 18). This choice also provides a better wall-normal resolution, which is particularly beneficial in simulations of turbulent flows. For full details of the IB method, the reader is referred to Nicolaou et al. (2015).

## 2.2. Particle tracking

A Eulerian–Lagrangian approach is adopted to model the particle transport and deposition. The aerosol/air mixture is a dilute dispersed flow with particle volume fraction,  $\alpha_p < \mathcal{O}(10^{-6})$ . It therefore lies in the one-way coupling regime: the flow affects the particles, but the effect of the particles on the flow is negligible (Elghobashi, 1994). Additionally, inter-particle interactions can be neglected. The aerosol particles are tracked through the flow field by solving their equation of motion:

$$m_p \frac{d\mathbf{u}_p}{dt} = \sum \mathbf{F}, \quad (5)$$

where  $m_p$  and  $\mathbf{u}_p$  denote the particle mass and velocity respectively and  $\sum \mathbf{F}$  represents all the forces acting on the particle. For particles in the micrometer range, the dominant forces are the aerodynamic drag and gravity. The particles are assumed to be spherical, which is justified for small liquid aerosols. For dry powder aerosols, the drag acting on the particles is similar to that on a sphere since the particles are compact. Hence, the balance of forces acting on the particles is given by

$$m_p \frac{d\mathbf{u}_p}{dt} = \frac{3}{4} \frac{\rho_f m_p}{\rho_p d_p} C_D |\mathbf{u}_f - \mathbf{u}_p| (\mathbf{u}_f - \mathbf{u}_p) + m_p \mathbf{g} \frac{\rho_p - \rho_f}{\rho_p}, \quad (6)$$

where  $\rho_f$  is the fluid density and  $C_D$  is the drag coefficient. The correlation proposed by Schiller and Naumann (1933) is adopted for the drag coefficient:

$$C_D = \frac{24}{Re_p} (1 + 0.15 Re_p^{0.687}), \quad (7)$$

where  $Re_p$  is the particle Reynolds number:

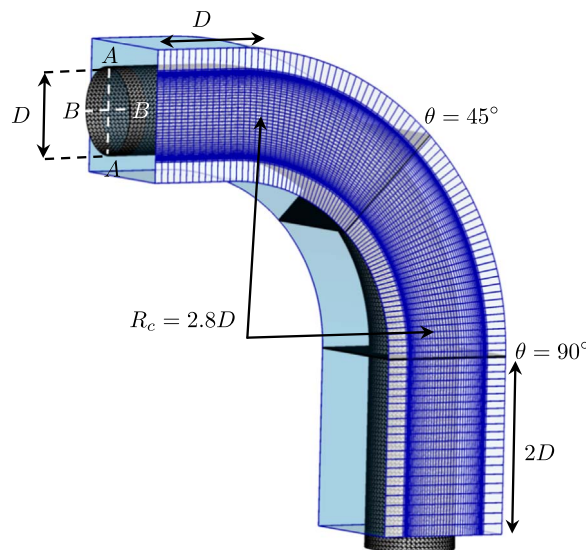


**Fig. 1.** The geometry and grid employed for the curved pipe simulations. Every eighth gridline has been plotted. A–A is the diameter of the cross section at the symmetry plane and B–B is the diameter perpendicular to it.

$$Re_p = \frac{\rho_f d_p |\mathbf{u}_f - \mathbf{u}_p|}{\mu_f}. \quad (8)$$

Note that in the canonical pipe configuration in Section 3.1, gravity is not considered in keeping with the setup of earlier studies. It is, however, retained in the extrathoracic airways.

Integration of the particle equations of motion is performed using a fourth-order Runge–Kutta (RK4) scheme implemented in physical space. The fluid velocity at the particle location, required for the computation of the drag force, is evaluated using trilinear interpolation of the Cartesian velocities in computational space, where the grid is uniform and orthogonal. In order to determine the host cell  $\{i, j, k\}$ , of a particle on a curvilinear grid, a local search method combined with tetrahedrization (Shirayama, 1993) is adopted. Finally, deposition is assumed once a particle comes into contact with the wall of the geometry.

### 2.3. The effective Stokes number

An important parameter which characterizes the motion of particles is the non-dimensional Stokes number, defined as the ratio of the particle response time,  $\tau_p$ , to the characteristic time scale of the flow,  $\tau_f$ :

$$Stk \equiv \frac{\tau_p}{\tau_f} \quad \text{where} \quad \tau_p = \frac{\rho_p d_p^2}{18\mu_f}. \quad (9)$$

For small Stokes numbers,  $Stk \ll 1$ , the particle velocity is nearly that of the fluid and the particles follow the streamlines. As the Stokes number exceeds unity, the particle motion becomes increasingly insensitive to the flow, and particles deviate from the streamlines. This suggests that the larger the Stokes number the more likely a particle will undergo inertial impaction onto the airway walls. Typically a reference Stokes number is defined, based on the characteristic flow velocity  $U$  and length scale  $D$ :

$$Stk_{ref} \equiv \frac{\rho_p d_p^2 U}{18\mu_f D}. \quad (10)$$

In the extrathoracic airways,  $U$  is often chosen to be the mean flow velocity and  $D$  the mean airway diameter.

Here we propose the use of a Stokes number based on the local flow properties (Trujillo & Parkhill, 2011). This local, or instantaneous, Stokes number is defined as

$$Stk_{inst} \equiv \frac{\rho_p d_p^2}{18\mu_f} \max_i \| \Lambda_i \| \quad (i = 1, 2, 3), \quad (11)$$

where  $\Lambda_i$  are the eigenvalues of the velocity gradient tensor.

In order to understand the origin of  $Stk_{inst}$ , the eigenvalues of the inertial and passive particle advection equations are compared (Trujillo & Parkhill, 2011). These equations are, respectively,

$$\frac{d\mathbf{u}_p}{dt} = \frac{\mathbf{u}_f - \mathbf{u}_p}{\tau_p} + \mathbf{g} \frac{\rho_p - \rho_f}{\rho_p}, \quad (12)$$

$$\mathbf{u}_p = \mathbf{u}_f. \quad (13)$$

The Lagrangian equivalents of Eqs. (12) and (13) are

$$\frac{d^2}{dt^2} \Delta \mathbf{x}_p + \frac{1}{\tau_p} \frac{d}{dt} \Delta \mathbf{x}_p = \frac{\mathbf{u}_0 + \nabla \mathbf{u}_0 \cdot \Delta \mathbf{x}_p + t \frac{d}{dt} \mathbf{u}_0}{\tau_p} + \mathbf{g} \frac{\rho_p - \rho_f}{\rho_p}, \quad (14)$$

$$\frac{d}{dt} \Delta \mathbf{x}_p = \mathbf{u}_0 + \nabla \mathbf{u}_0 \cdot \Delta \mathbf{x}_p + t \frac{d}{dt} \mathbf{u}_0, \quad (15)$$

where  $\Delta \mathbf{x}_p$  is the displacement of the particle from an initial point,  $\mathbf{x}_p(0)$ , and  $\mathbf{u}_0$  is the initial fluid velocity,  $\mathbf{u}_f(\mathbf{x}_p(0), 0)$ .

The eigenvalues of the passive system,  $\{\Lambda_1, \Lambda_2, \Lambda_3\}$ , are simply the eigenvalues of the velocity gradient tensor,  $\nabla \mathbf{u}_f$ . The eigenvalues of the inertial system are given by

$$\lambda_{1,2} = \frac{-1 \pm \sqrt{1 + 4\Lambda_1 \tau_p}}{2\tau_p}, \quad \lambda_{3,4} = \frac{-1 \pm \sqrt{1 + 4\Lambda_2 \tau_p}}{2\tau_p}, \quad \lambda_{5,6} = \frac{-1 \pm \sqrt{1 + 4\Lambda_3 \tau_p}}{2\tau_p}. \quad (16)$$

If  $|\Lambda_i \tau_p| \leq 1/4$ , a Taylor expansion yields

$$\sqrt{1 + 4\Lambda_i \tau_p} = 1 + 2\Lambda_i \tau_p - \frac{(4\Lambda_i \tau_p)^2}{8} + \dots = 1 + P(\Lambda_i \tau_p). \quad (17)$$

Discarding the initial transient ( $t \gtrsim 3\tau_p$ ) and substituting (17) into (16) yields

$$\lambda_1 = \frac{P(\Lambda_1 \tau_p)}{2\tau_p}, \quad \lambda_3 = \frac{P(\Lambda_2 \tau_p)}{2\tau_p}, \quad \lambda_5 = \frac{P(\Lambda_3 \tau_p)}{2\tau_p}. \quad (18)$$

The ratios of the inertial and passive time scales are given by

$$\frac{1/\lambda_1}{1/\Lambda_1} = \frac{2\tau_p/P(\Lambda_1\tau_p)}{1/\Lambda_1}, \quad \frac{1/\lambda_3}{1/\Lambda_2} = \frac{2\tau_p/P(\Lambda_2\tau_p)}{1/\Lambda_2}, \quad \frac{1/\lambda_5}{1/\Lambda_3} = \frac{2\tau_p/P(\Lambda_3\tau_p)}{1/\Lambda_3}. \quad (19)$$

For each ratio, as  $\Lambda_i\tau_p$  becomes smaller  $P(\Lambda_i\tau_p) \rightarrow 2\Lambda_i\tau_p$ , resulting in matching timescales. In this limit, inertial particles adopt passive advection. The maximum value of the modulus of the eigenvalues is considered as the limiting factor. Therefore the instantaneous Stokes number is defined as

$$Stk_{inst} \equiv \max_i \| \Lambda_i \| \tau_p \quad (i = 1, 2, 3). \quad (20)$$

An effective Stokes number can be computed as the time-average of the instantaneous value:

$$Stk_{eff} = \frac{1}{T} \int_0^T Stk_{inst} dt, \quad (21)$$

where  $T$  is the period during which a particle remains in the flow. It is also helpful to define the mean effective Stokes number for a population of particles, which is given by

$$\overline{Stk_{eff}} = \frac{1}{n_p} \sum_{n=1}^{n_p} Stk_{eff}(n), \quad (22)$$

where  $n_p$  is the size of the population.

### 3. Results and discussion

#### 3.1. 90° circular bend

We first consider flow and particle deposition in a circular pipe with a 90° bend, which resembles the geometry of the extrathoracic airways. The flow is characterized by the Dean number, which provides a measure of the inertial and centrifugal forces relative to the viscous forces. The Dean number is  $De \equiv Re_D(D/2R_c)^{1/2}$ , where  $Re_D \equiv \rho_f UD/\mu_f$  is the Reynolds number,  $D$  is the pipe diameter and  $R_c$  is the radius of curvature of the pipe axis. The radius of curvature was set to  $R_c = 2.8D$ , and two cases were considered: (i) laminar flow at  $Re_D=1000$  and (ii) turbulent flow at  $Re_D=10,000$ , which correspond to  $De=422.6$  and  $De=4226$ , respectively.

The IB method, rather than a cylindrical body-fitted grid, was adopted for this configuration and serves as a validation step as well as a canonical test case before proceeding to the airways. A curvilinear grid with  $769 \times 385 \times 1025$  points in the streamwise  $\xi$ , cross-stream  $\eta$ , and spanwise  $z$ , directions was employed. The grid spacing in wall-units for the high Reynolds number case was  $3.93 < \Delta\xi^+ < 9.62$  (near the outflow),  $0.50 < \Delta\eta^+ < 3.00$ ,  $\Delta z^+ = 0.91$ , which is sufficient to resolve the turbulence (Eggels et al., 1994; Kim, Moin, & Moser, 1987). The grid and domain setup are shown in Fig. 1. For the laminar flow case, a parabolic inflow profile was prescribed at the inlet, and a convective boundary condition was adopted at the exit for all flow conditions. For the turbulent flow simulation, a time-dependent inflow turbulent profile was obtained from a precursor direct numerical simulation of pipe flow at  $Re_D=10,000$ . The length of the pipe in the precursor simulation was  $L_x = 25D$ . Taylor hypothesis was invoked to transform the axial coordinate into time at the inlet plane of the main bent-pipe simulation.

Particles were released at the inlet plane at random locations drawn from a uniform distribution and tracked through the flow field until they exited the bend or deposited on the wall. The initial particle velocity was set equal to the fluid velocity at the release location. The density ratio was set to  $\rho_p/\rho_f = 755$  and gravitational acceleration was neglected for comparison with studies in the literature (Breuer, Baytekin, & Matida, 2006; Cheng & Wang, 1981; Tsai & Pui, 1990). The Stokes number was varied from  $Stk=0.001$  to 1.4, and approximately 100,000 particles were tracked for each size. In the laminar case, the flow is steady and therefore particle tracking is computationally efficient as it is performed on a frozen field. In the turbulent case, particles were released into the flow at regular intervals,  $\Delta t_{release} = 0.0375D/U$ , during a period of 2.5 time units (half a flow-through time) in order to ensure results were independent of release time. The main flow and particle parameters adopted in each case are summarized in Table 1.

**Table 1**

Flow and particle parameters in the curved pipe simulations.

Parameter	Laminar case	Turbulent case
$Re_D$	1000	10,000
$De$	422.6	4226
$Stk_{ref} \times 10^2$	{1, 2, 4, 6, 8, 10, 14, 16, 20, 28, 34, 40, 50, 60, 80, 100, 120, 140}	{1, 5, 10, 20, 30, 40, 50, 60, 80, 100,120,135,150}
$\rho_p/\rho_f$	755	755

3.1.1. Laminar flow

The velocity fields in two cross-flow planes are shown in Fig. 2. The contours represent the streamwise velocity and the streamlines are constructed from the in-plane components. At  $\theta = 45^\circ$  the secondary flow is clearly visible in the streamlines (Fig. 2a), in the form of a pair of symmetric counter-rotating vortices. The streamwise velocity contours show that the high velocity fluid is shifted from the centre of the duct towards the outer wall (Fig. 2c). The secondary flow advects this high-momentum fluid along the side walls towards the inner wall. Further along the bend, at  $\theta = 90^\circ$ , the trend intensifies. The strong secondary flow causes the fluid to swirl, and three pairs of vortices are visible (Fig. 2b). These results are in agreement with theoretical predictions for large Dean numbers,  $De \geq 370$  (Pui, Romay-Novas, & Liu, 1987) and numerical results in the literature (Breuer et al., 2006; Pilou et al., 2011). Similar dynamics have also been observed in realistic extrathoracic airways, in particular the presence of strong secondary flow and the formation of Dean-like vortices in some subjects (Nicolaou & Zaki, 2013).

Radial profiles of streamwise velocity at the two streamwise locations in the symmetry plane (A–A) and perpendicular to the symmetry plane (B–B) are shown in Fig. 3, and are compared to numerical results from the literature (Pilou, Tsangaris, Neofytou, Housiadas, & Drossinos, 2011). In addition to our fine-grid resolution, the comparison also includes a coarser grid simulation with 6% of the total number of grid points ( $19 \times 10^6$  versus  $300 \times 10^6$  grid points). Grid independence is demonstrated, and excellent agreement is observed between our immersed-boundary simulation and the body-fitted data.

The focus is now placed on the transport and fate of particles that are released in the flow. They will be classified into two groups: (i) deposited and (ii) not deposited; where the undeposited population can be further sub-divided into (iia) particles that remain in the flow domain and (iib) particles that have exited the geometry. Fig. 4 shows the deposition efficiency versus reference Stokes number. The percentages of particles that remain and that exit the pipe within 40 convective time units,  $t = 40D/U$ , are also shown. The blue line represents all the particles that have not deposited, i.e. particles that have exited as well as those remaining in the flow. Here the reference Stokes number is based on the mean bulk velocity and radius of the pipe,  $Stk_{ref} = \frac{\rho_p d_p^2 U}{18\mu_f D/2}$ . A trend similar to the S-curve in the extrathoracic airways is observed. Three regimes can be distinguished: (i) low  $Stk_{ref}$  regime where there is a weak

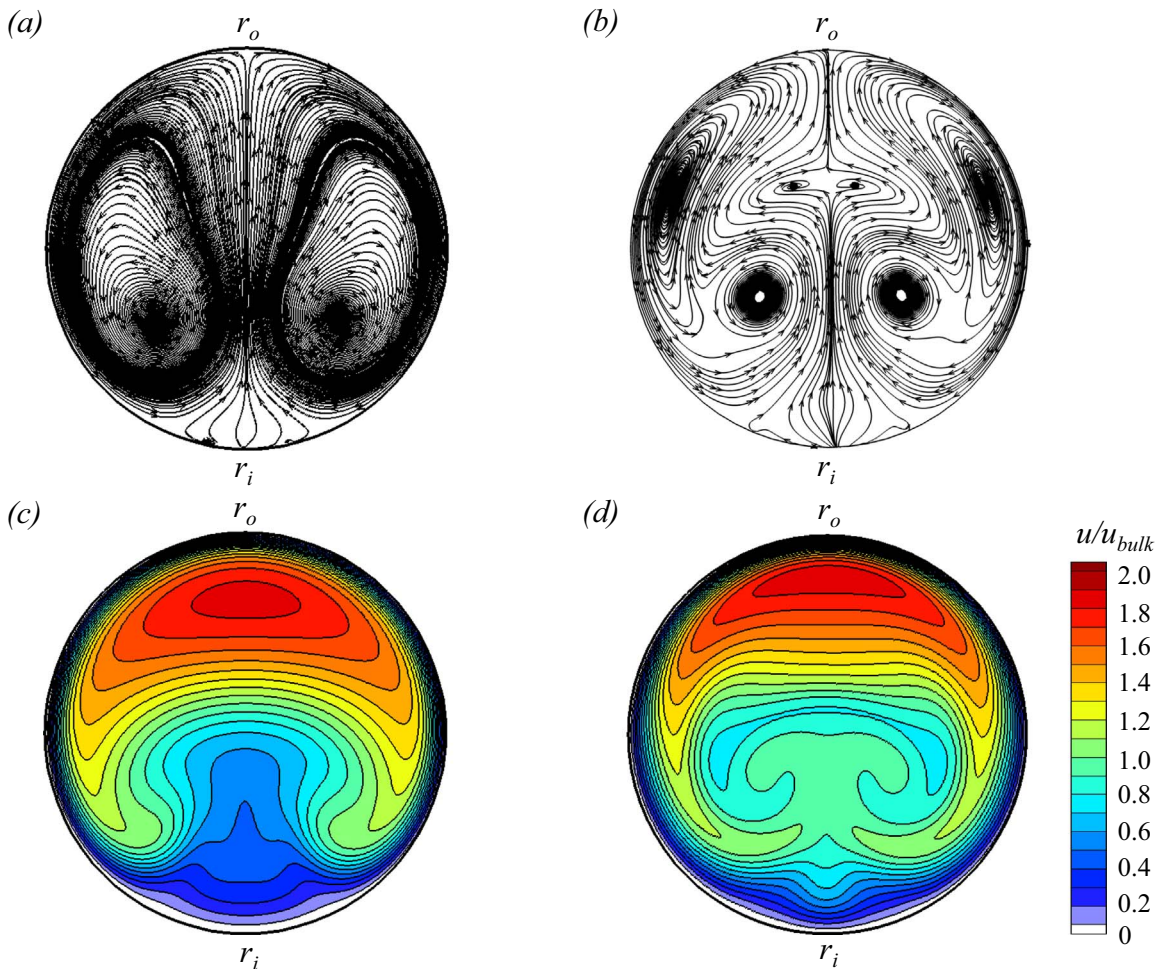
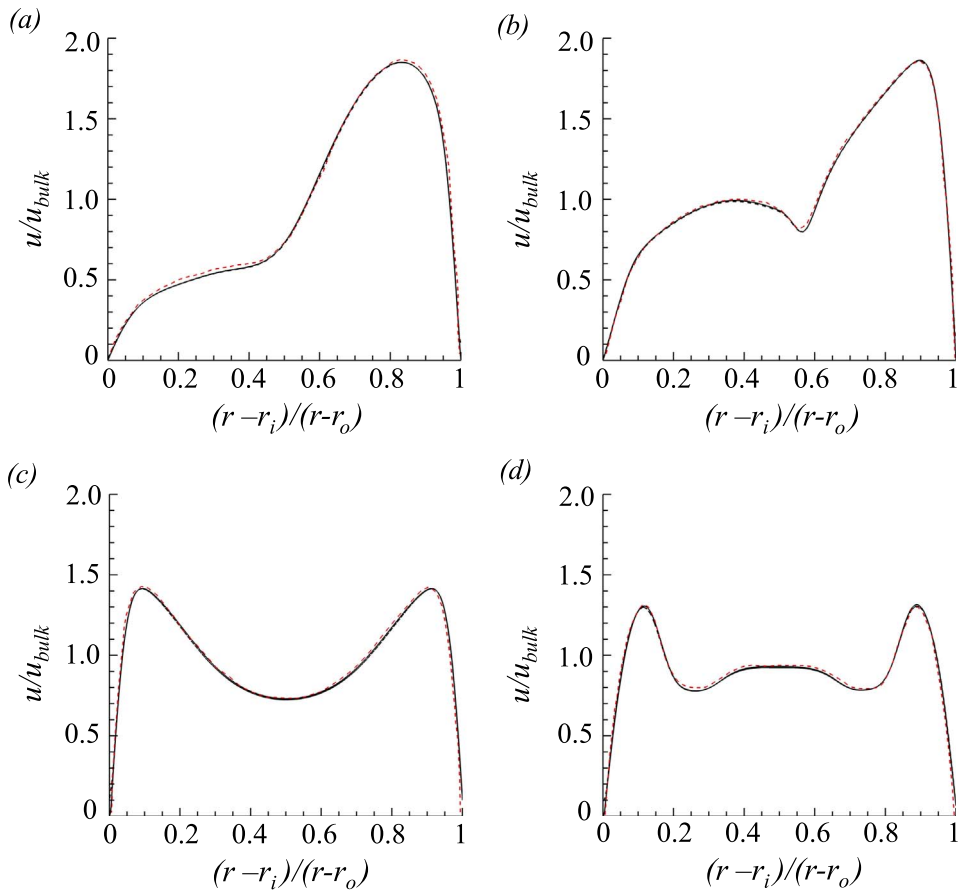
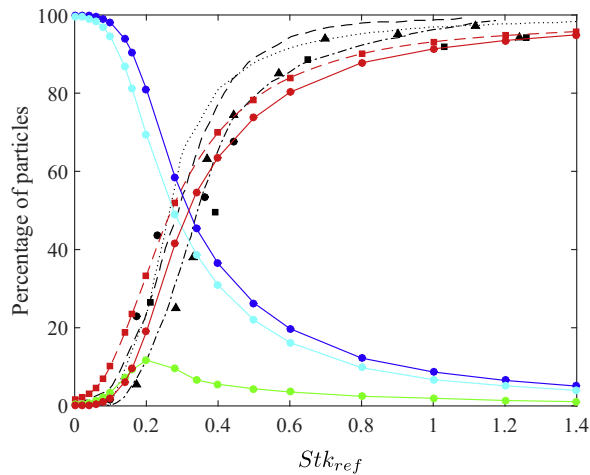


Fig. 2. Laminar flow in curved pipe at  $Re_D=1000$ : Secondary flow streamlines (top) and streamwise velocity contours (bottom) at two cross-flow planes inside the bend: (a and c)  $\theta = 45^\circ$  and (b and d)  $\theta = 90^\circ$ .



**Fig. 3.** Laminar flow in curved pipe at  $Re_D=1000$ : Profiles of velocity magnitude at (a and c)  $\theta = 45^\circ$  and (b and d)  $\theta = 90^\circ$  cross-flow planes inside the bend, along the diameters A–A (top) and B–B (bottom). - - - coarse grid simulation ( $513 \times 193 \times 193$  points); — fine grid simulation ( $769 \times 385 \times 1025$  points); and - · - · Pilou et al. (2011).



**Fig. 4.** Laminar flow in curved pipe at  $Re_D=1000$ : Deposition efficiency versus reference Stokes number. - - - coarse grid simulation; — fine grid simulation; - - - Tsai and Pui (1990); ··· Breuer et al. (2006); ···· Cheng and Wang (1981); ▲; ■; • Pui et al. (1987). Percentage of particles — not deposited; — still in the flow domain; — that have exited the pipe.

dependence on the Stokes number; (ii) intermediate regime where there is a marked increase in deposition with Stokes number; and (iii) high  $Stk_{ref}$  regime where deposition plateaus as particles display ballistic behaviour and therefore the majority deposit. Comparison of the deposition efficiency results from the coarse-grid and fine-grid simulations shows that particles in the low-to-intermediate Stokes number regime are most sensitive to the grid resolution, and the results demonstrate good agreement with

numerical and experimental studies in the literature.

Particle trajectories and the deposited particles are shown in Figs. 5 and 6, and are coloured by their instantaneous Stokes number. The two figures correspond to  $Stk_{ref} = 0.2$  and  $Stk_{ref} = 1.0$ . For both particle sizes, an increase in Stokes number is observed as the particles approach the bend and the highest instantaneous Stokes numbers are experienced along the outer wall (Figs. 5a and 6a). Inside the bend, the light particles ( $Stk_{ref} = 0.2$ ) move along the side walls from the outer to the inner wall due to the effect of the secondary flow (Fig. 5a–c). Deposition is shown to occur in the regions of high instantaneous Stokes number: the outer bend due to impaction and on the side walls due to the influence of the secondary flow (Fig. 5d–f). The heavier particles ( $Stk_{ref} = 1.0$ ) experience a more significant shift towards the outer wall due to their high inertia. This region also hosts the highest Stokes numbers (Fig. 6a–c). Therefore, high deposition via impaction occurs along the outer wall, where the particles' Stokes numbers are highest (Fig. 6d–f).

The distribution of the effective Stokes number is examined in Fig. 7, where particles are visualized at the inlet plane, coloured by their  $Stk_{eff}$ . The results are reported for three reference values of  $Stk_{ref}$ , or equivalently particle sizes. At left all particles are plotted, while at right only the deposited particles are displayed. At  $Stk_{ref} = 0.2$ , qualitative agreement of the penetration/deposition regions with those by Breuer et al. (2006) is observed. The discrepancy between the two results can be attributed to the different deposition criteria and particle-tracking schemes adopted. A significant spread in effective Stokes number is observed across all three particle sizes. Depending on their initial release position, particles experience very different Stokes numbers as they are advected through the flow. A clear correlation between high  $Stk_{eff}$  and deposition is also observed. This knowledge is beneficial in selecting optimal release locations in order to minimize deposition.

Further detail on the distribution of the effective Stokes number for each particle size can be gathered from the probability density functions (pdf) of  $Stk_{eff}$  shown in Fig. 8. It is evident that the bimodal distribution of the total set of particles is composed of two distinct pdfs: (i) particles that deposit and (ii) particles that do not deposit as shown in red and blue, respectively. The mean effective Stokes number for the deposited particles,  $\overline{Stk_{eff}^d}$ , is higher than that for particles that remain undeposited,  $\overline{Stk_{eff}^f}$ , which reaffirms the correlation between high  $Stk_{eff}$  and deposition. The difference between the two values increases as particle size decreases.

Finally, the deposition efficiencies versus effective Stokes number for each particle size are shown in Fig. 9. The plots display a much steeper rise compared to the original S curve based on  $Stk_{ref}$ , which is also shown in the figure for comparison. Two main regimes can be observed: low and high deposition. Each particle size has its own S-curve of deposition versus  $Stk_{eff}$ , which is

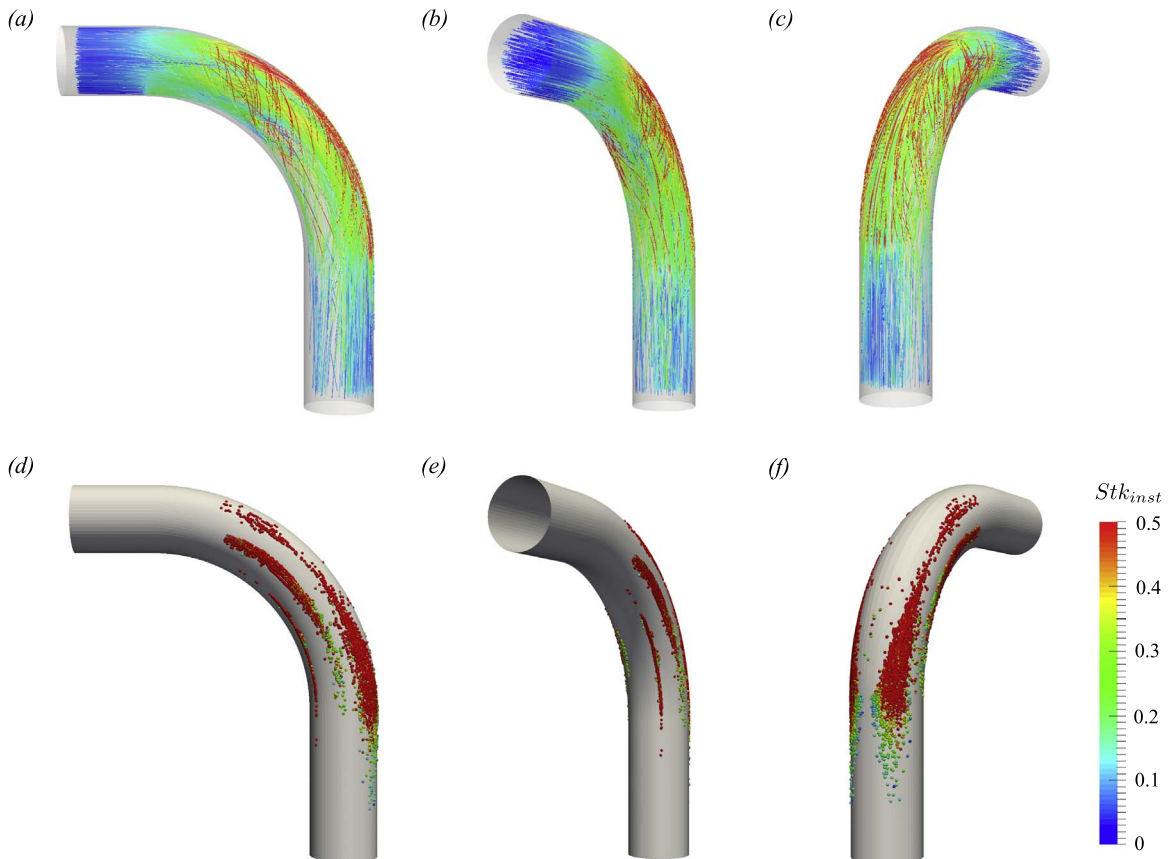


**Fig. 5.** Laminar flow in curved pipe at  $Re_D=1000$ : Particle trajectories (a–c) and deposited particles (d–f) coloured by their instantaneous Stokes number for  $Stk_{ref} = 0.2$ . (For interpretation of the references to colour in this figure caption, the reader is referred to the web version of this paper.)

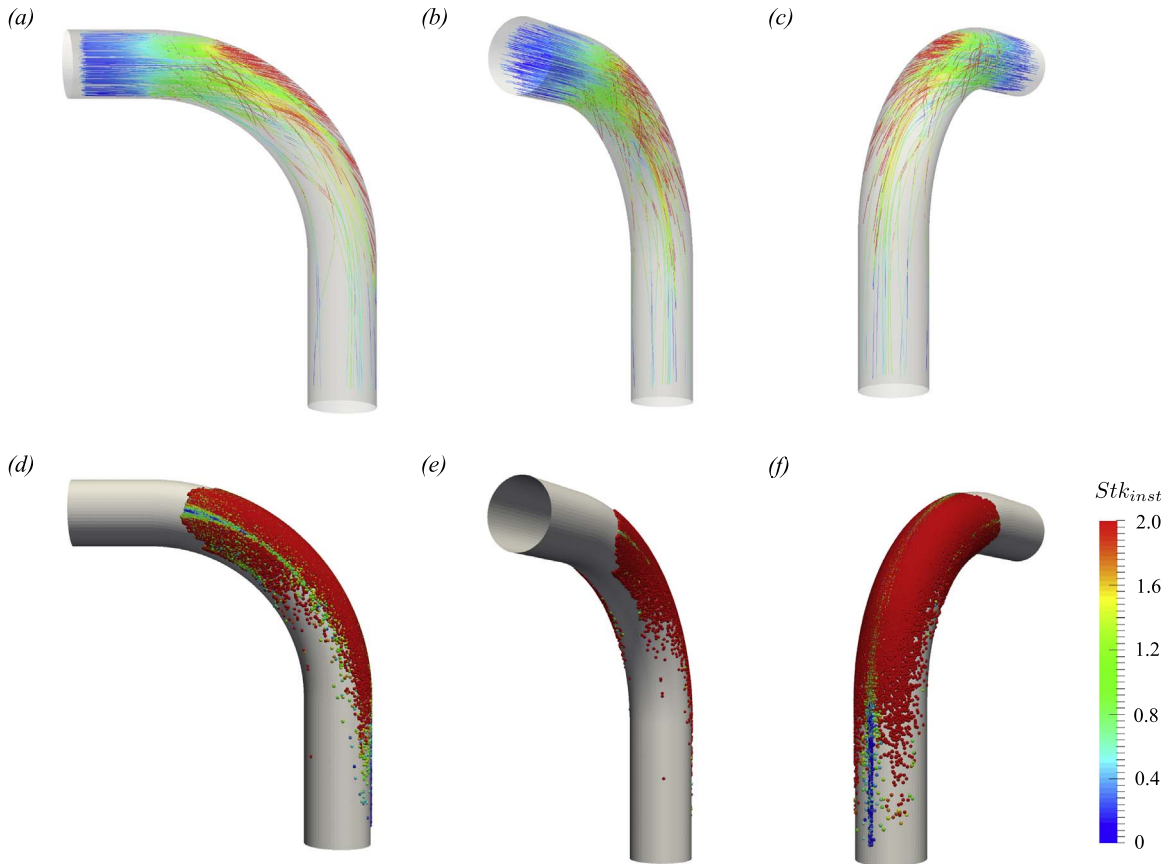


**Fig. 6.** Laminar flow in curved pipe at  $Re_D=1000$ : Particle trajectories (a–c) and deposited particles (d–f) coloured by their instantaneous Stokes number for  $Stk_{ref} = 1.0$ . (For interpretation of the references to colour in this figure caption, the reader is referred to the web version of this paper.)

reflective of the different particle trajectories depending on their insertion location. As size increases, this curve shifts to higher  $Stk_{eff}$ . Along each  $Stk_{eff}$  curve, the particle relaxation time remains constant while the flow time scale varies, and in this manner the definition of  $Stk_{eff}$  takes into account the effect of the flow history on deposition.

### 3.1.2. Turbulent flow

We now turn to the turbulent-flow configuration at  $Re_D=10,000$ . Beyond the initial transient period, statistical averaging of flow quantities is performed for 20 convective time units. Figs. 10a and b show the streamlines of the time-averaged flow and contours of the mean pressure in the central spanwise plane. These results are in very good agreement with the literature (see e.g. Breuer et al., 2006). A snapshot of the instantaneous velocity magnitude is shown in Fig. 10c.

The mean secondary-flow streamlines in two cross-flow planes inside the bend are shown in Fig. 11. Note that the flow does not exhibit perfect symmetry about the vertical axis. The strength of Dean vortices in turbulent flows varies with time, with each vortex dominating the secondary flow alternately. This oscillatory behaviour known as ‘swirl switching’ is at very low frequency and, as a result, a very long averaging period is required in order to obtain symmetric secondary-flow statistics. Nevertheless, the results in Fig. 11 show the main secondary flow structures, and a long averaging period is not needed in the present study where the focus is on particle trajectories and deposition rather than a statistical description of the flow field. At  $\theta = 45^\circ$  a pair of small vortex cells is observed at the inner radius, due to separation of the secondary boundary layer which can occur at high Dean numbers (Pui et al., 1987). Further along the bend, the centres of the main vortices shift towards the side walls as the high momentum fluid shifts closer to the outer wall and swirls along the side walls.

The deposition efficiency versus reference Stokes number at  $Re_D=10,000$  is shown in Fig. 12. The percentage of particles that remain in the flow and that have exited the pipe after 20 convective time units are also shown. Although the percentage of deposited particles follows a similar trend to the laminar case, some clear differences exist. The S-curve no longer has a flat section at low Stokes numbers, because deposition in this regime is higher by virtue of turbulent dispersion. Also, in the intermediate Stokes number regime, the slope is more gentle than in the laminar case. In this regime, deposition is due to both impaction and turbulent dispersion. Impaction, which is dominant, increases with particle size. On the other hand, deposition due to turbulent dispersion decreases with particle size resulting in a more gentle overall increase in deposition with particle size compared to the laminar case where deposition is via impaction alone. Since particle trajectories are strongly dependent on their insertion location and time in the

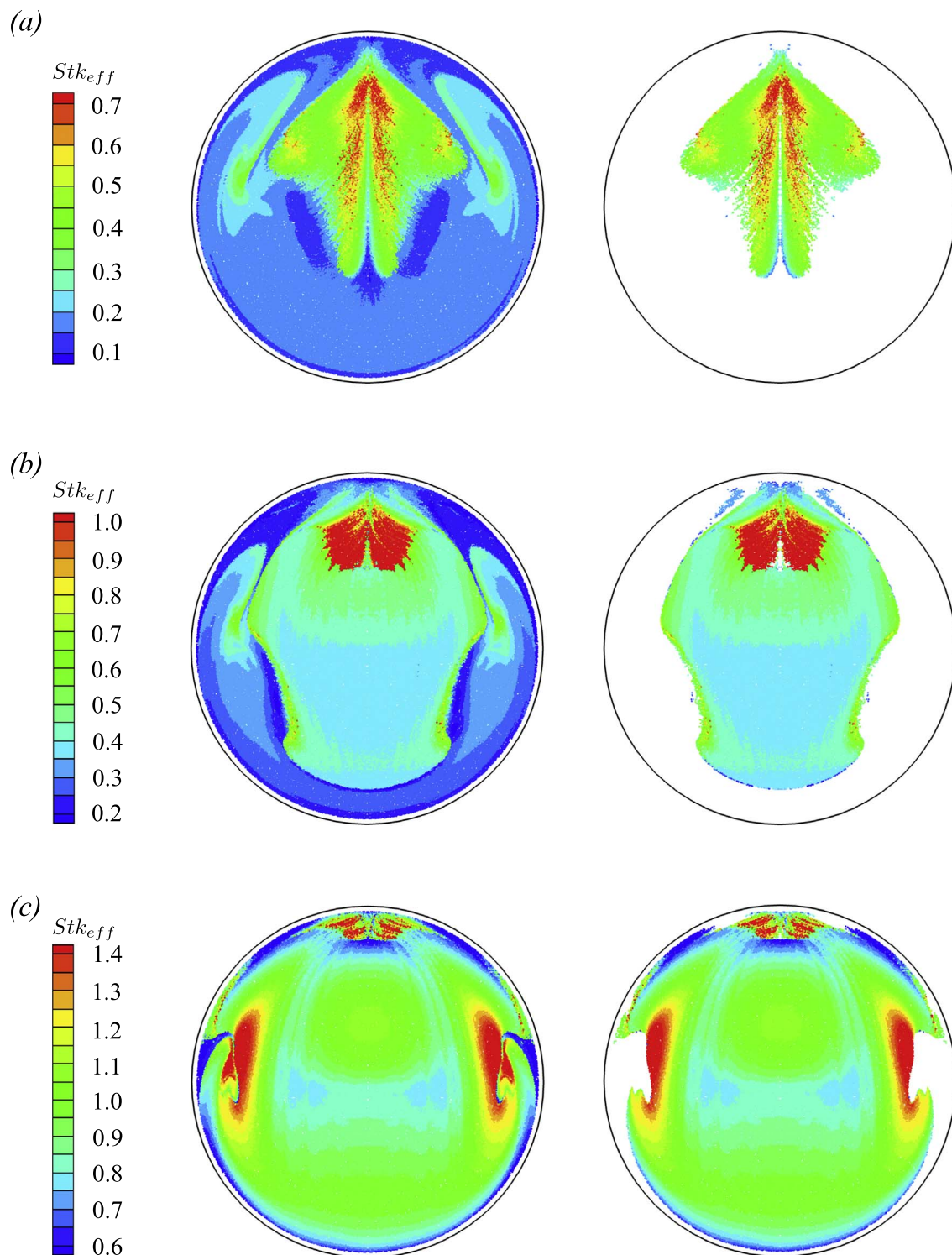


**Fig. 7.** Laminar flow in curved pipe at  $Re_D=1000$ : Particles at inlet coloured by effective Stokes number: (a)  $Stk_{ref} = 0.2$ ; (b)  $Stk_{ref} = 0.34$ ; and (c)  $Stk_{ref} = 1.0$ . On the left: all particles; on the right: deposited particles only. (For interpretation of the references to colour in this figure caption, the reader is referred to the web version of this paper.)

turbulent configuration, deposition patterns are expected to change appreciably relative to the earlier laminar conditions. The instantaneous and effective Stokes numbers provide an informative account of these changes.

Fig. 13 shows contours of  $|u|_{max}$  in the central spanwise plane and a cross-section near the inlet, along with the particle trajectories

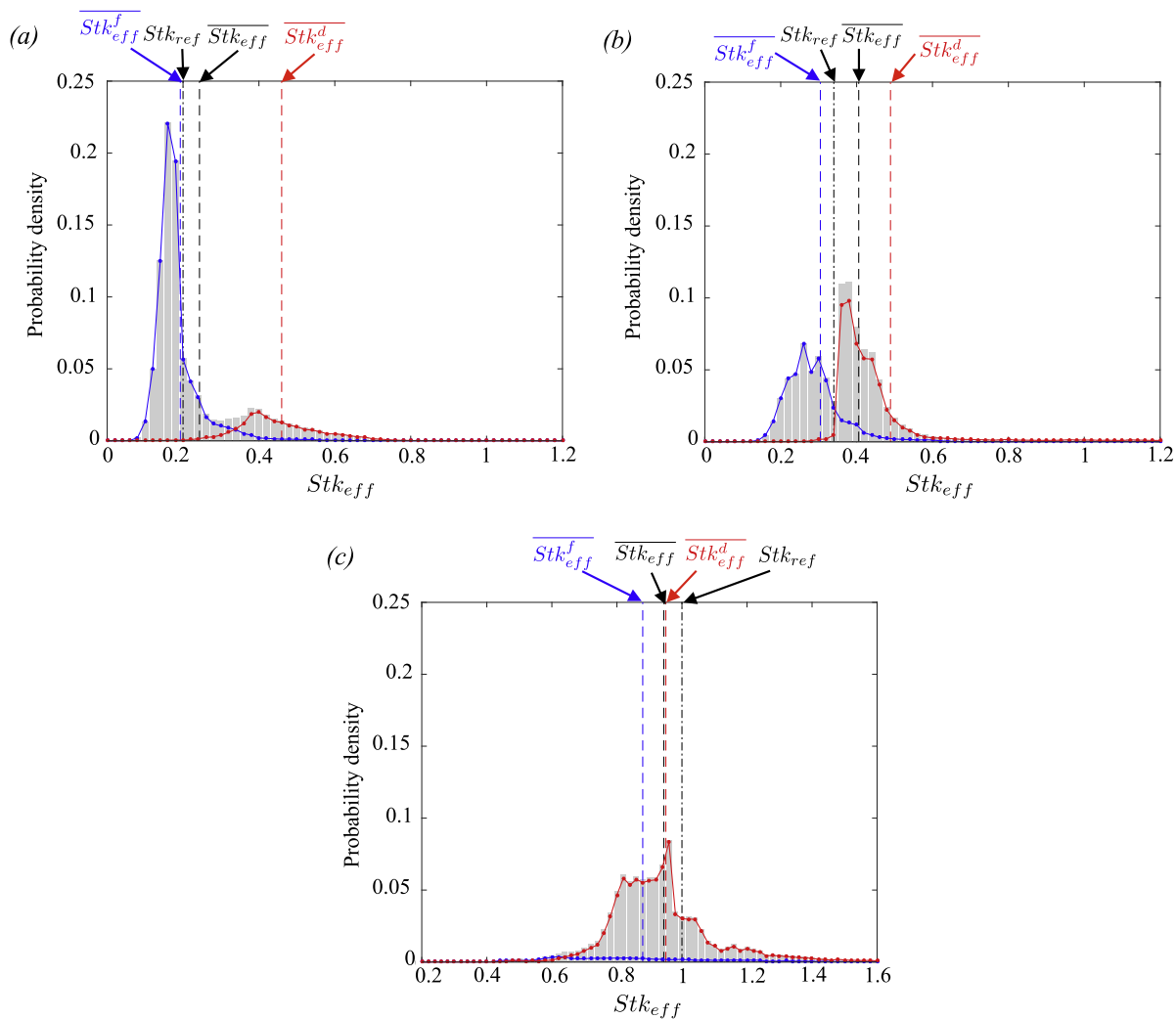


**Fig. 8.** Laminar flow in curved pipe at  $Re_D=1000$ : Pdf of effective Stokes number for (a)  $Stk_{ref} = 0.2$ ; (b)  $Stk_{ref} = 0.34$ ; (c)  $Stk_{ref} = 1.0$ . ■ All particles; — particles not deposited; and — deposited particles. Corresponding mean values:  $\overline{Stk_{eff}}$ ; - -  $Stk_{eff}^f$ ; and - -  $Stk_{eff}^d$ .

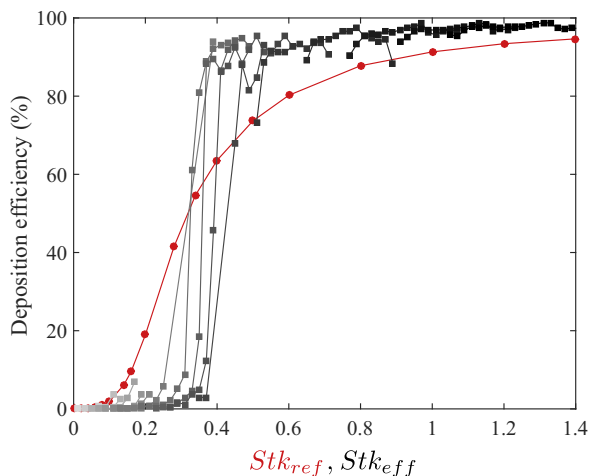


**Fig. 9.** Laminar flow in curved pipe at  $Re_D=10,000$ : Deposition efficiency versus Stokes number. ●  $Stk_{ref}$ ; ■ —  $Stk_{eff}$  curves for each particle size, in ascending order. (Particle sizes are listed in Table 1.).

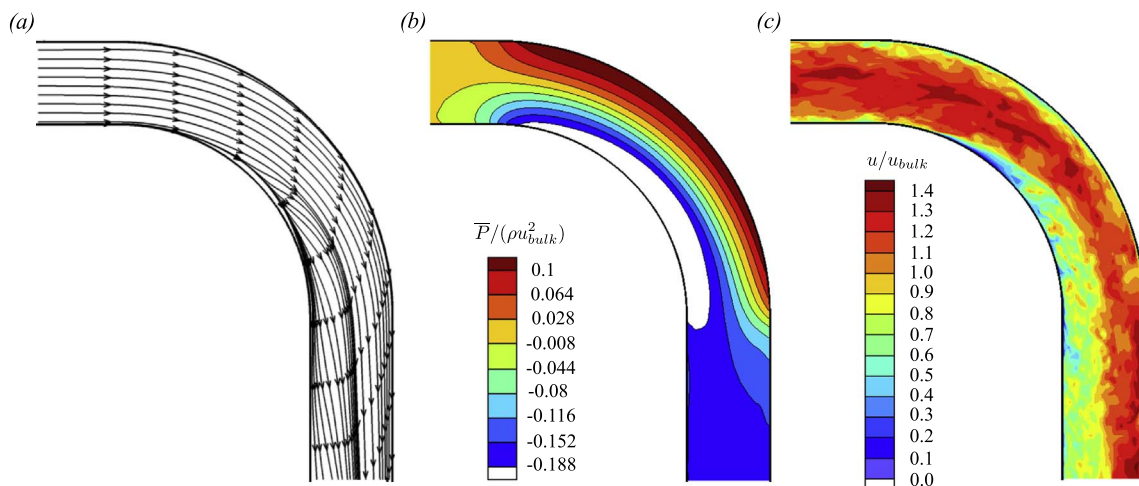


**Fig. 10.** Turbulent flow in curved pipe at  $Re_D=10,000$ : (a) Streamlines of the time-averaged flow; (b) contours of the mean pressure and (c) contours of the instantaneous velocity magnitude, in central spanwise plane.

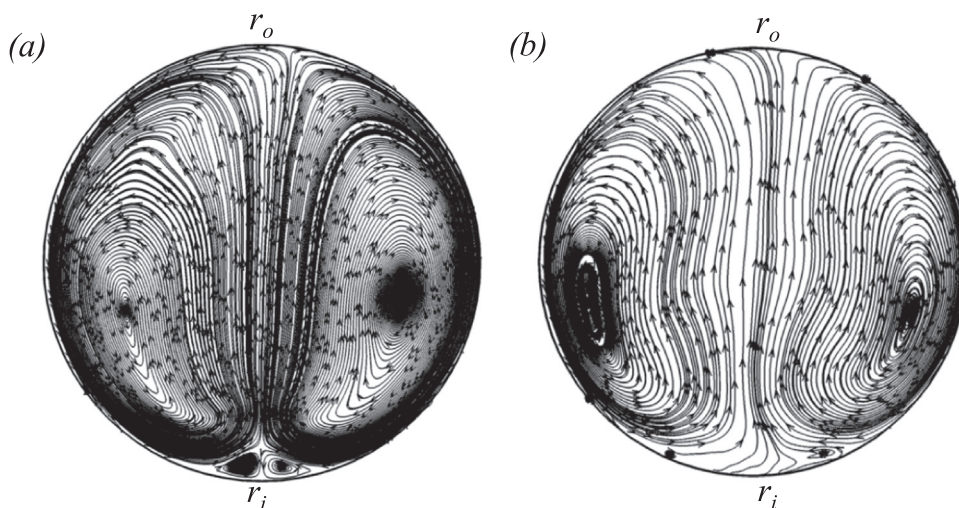


**Fig. 11.** Turbulent flow in curved pipe at  $Re_D=10,000$ : Secondary flow streamlines of time-averaged flow at two cross-flow planes inside the bend: (a)  $\theta = 45^\circ$  and (b)  $\theta = 90^\circ$ .

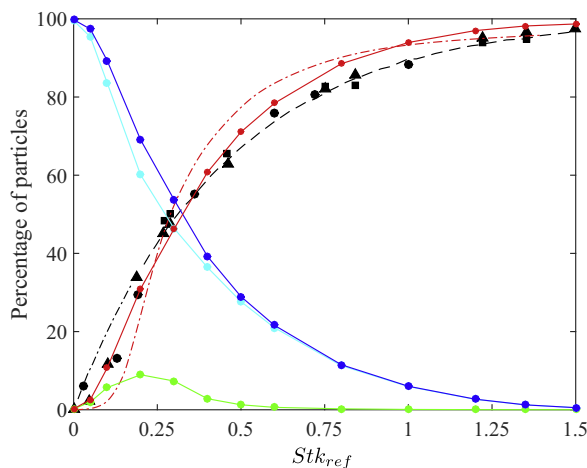


**Fig. 12.** Turbulent flow in curved pipe at  $Re_D=10,000$ : Deposition efficiency versus reference Stokes number: — current simulation;  $\blacktriangle$  LES (Breuer et al., 2006);  $\blacksquare$  • experimental data (Pui et al., 1987); - - curve fit (Pui et al., 1987);  $\square$  laminar case. Percentage of particles — not deposited; — still in the flow domain; — that have exited the pipe.

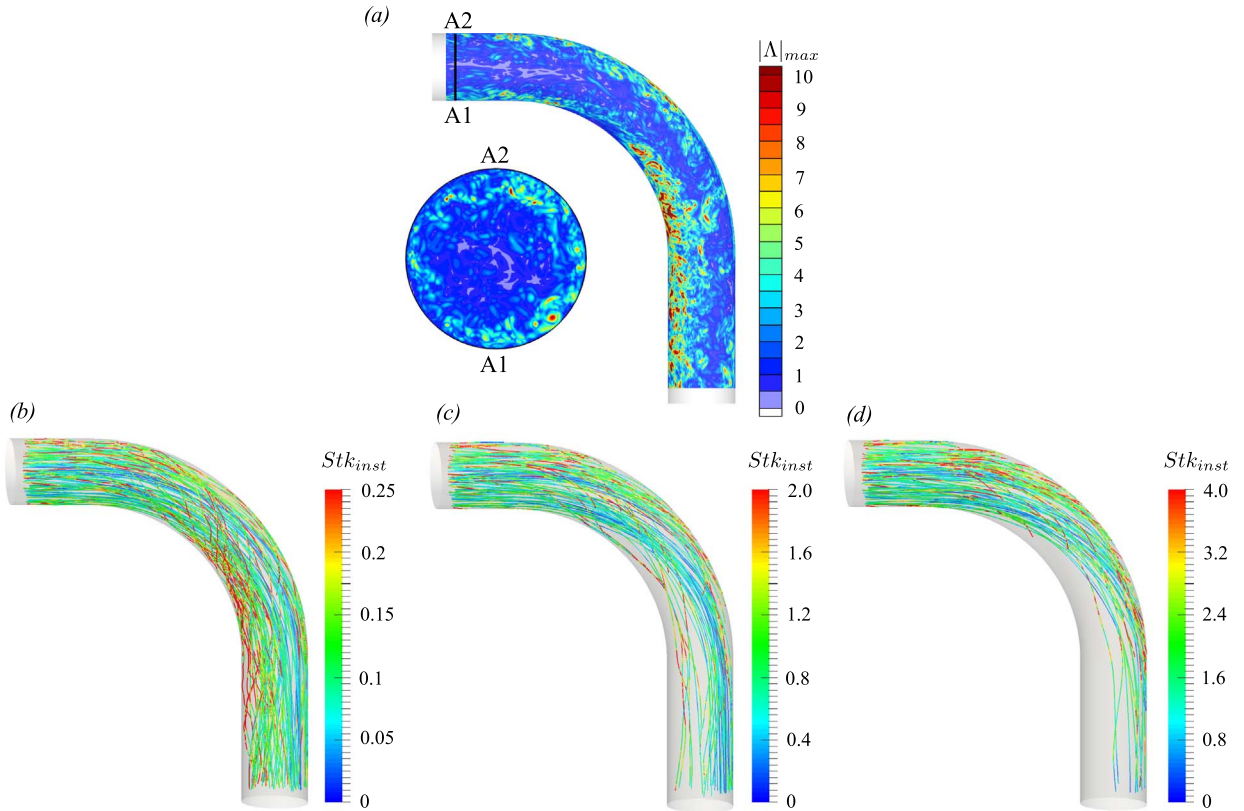


**Fig. 13.** Turbulent flow in curved pipe at  $Re_D=10,000$ : (a) Snapshot of  $|\Lambda|_{max}$  and particle trajectories coloured by their instantaneous Stokes number for (b)  $Stk_{ref} = 0.05$ ; and (c)  $Stk_{ref} = 0.4$  and (d)  $Stk_{ref} = 0.8$ . (For interpretation of the references to colour in this figure caption, the reader is referred to the web version of this paper.)

coloured by their instantaneous Stokes number for three different sizes of particles. As in the laminar case, the effect of the secondary flow on the trajectories is evident, with particles travelling from the outer to the inner radius along the side walls (Figs. 13b–d). In addition, the turbulent fluctuations also have a visible effect on the trajectories, in particular for the small particles (Fig. 13b). In terms of the evolution of the instantaneous Stokes numbers along the particle trajectories, clear differences with the laminar case are evident (cf. Figs. 5 and 6). In the laminar case  $Stk_{inst}$  is low at the inlet, increases as the particles approach the bend (with the highest  $Stk_{inst}$  observed near the outer wall) and then decreases again in the straight section of the bend. In the turbulent case, ‘streaks’ of high instantaneous Stokes number which begin at the inlet are observed near the wall. These correspond to the regions of highest  $|\Lambda|_{max}$  which occur within the buffer layer.

The deposition patterns for five different sized particles are shown in Fig. 14. The particles are coloured by their instantaneous Stokes number at the time of deposition. For small particle sizes (Fig. 14a) deposition is low, and occurs mainly on the side walls due to the effect of the secondary flow motion, similar to the small particles in laminar flow. As particle size increases, deposition increases along the outer wall of the bend as particle inertia increases and particles deposit in this region via impaction. Along the inner wall of the bend, there is a thin strip of negligible deposition for all particle sizes. This zone was also observed by Breuer et al. (2006) and was attributed to the pair of small counter-rotating vortices at the inner radius.

Next we examine the influence of release location on the effective Stokes number and deposition. Fig. 15 (left column) shows contours of effective Stokes number at the inlet location for four different sizes of particles. For all sizes, particles released near the top and side walls experience much higher  $Stk_{eff}$  than those released elsewhere at the pipe inlet. This is due to the combined effect of the high- $Stk_{inst}$  streaks near the walls, observed in Fig. 13, and the centrifugal force. Although in a straight pipe the distribution of  $Stk_{eff}$  should be axisymmetric, in the present setting particle trajectories shift towards the outer wall due to the bend. Therefore, particles released near the inner wall will be advected through the pipe core inside the bend where flow timescales are larger (or  $Stk_{inst}$  are smaller), resulting in lower  $Stk_{eff}$  compared to those particles released near the outer and side walls.

Contours of deposition and penetration fraction plotted at the particles’ inlet locations are shown in the middle and right columns of Fig. 15 respectively. These are very different from the laminar case where the deposition/penetration regions were sharply defined; the differences are due to turbulent dispersion. The highest levels of deposition across all particle sizes, occur when particles are released in the top half of the pipe inlet. This is the region where effective Stokes numbers are higher, and where high  $Stk_{inst}$  streaks are observed (Fig. 13).

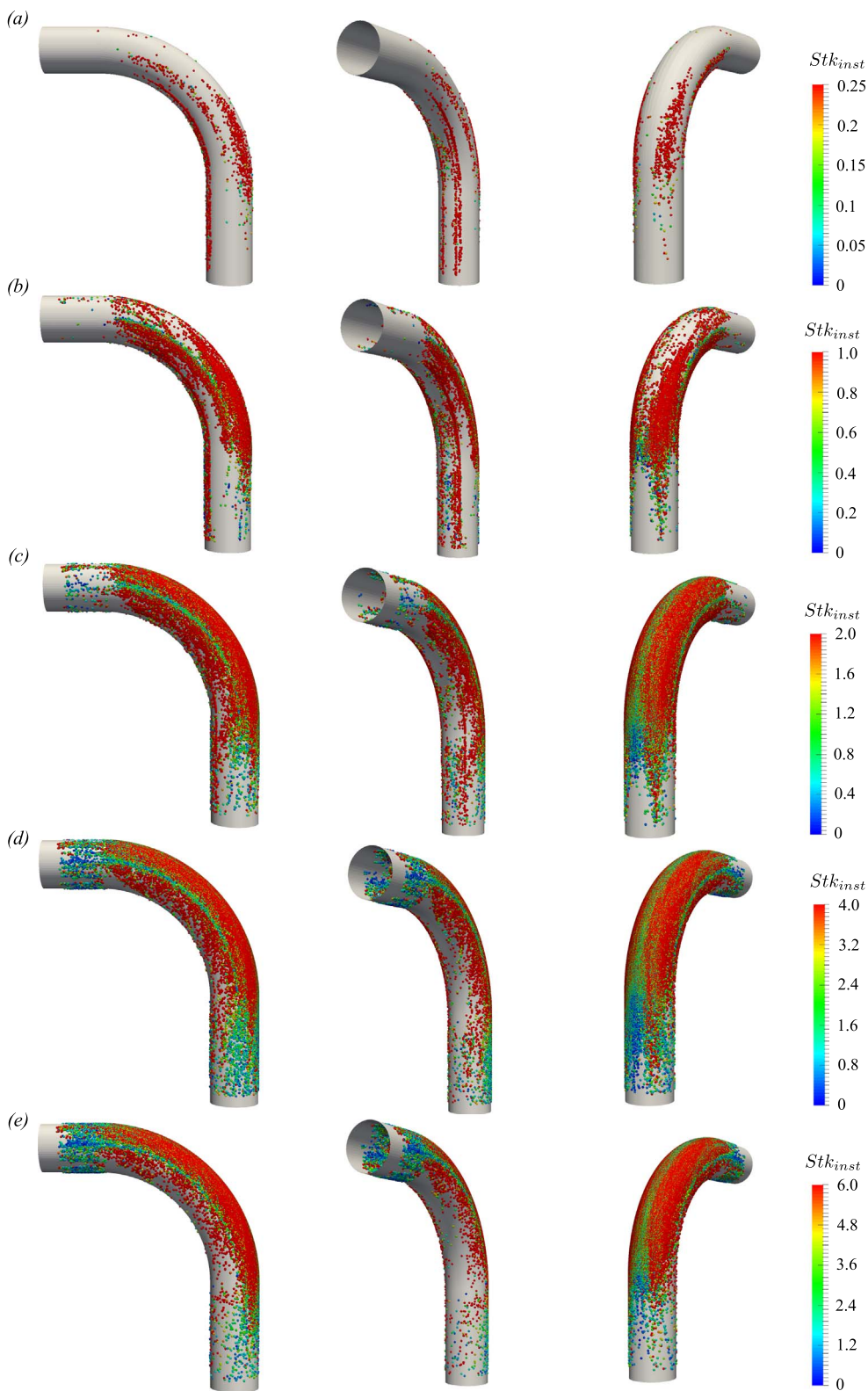


**Fig. 14.** Turbulent flow in curved pipe at  $Re_D=10,000$ : Deposited particles coloured by their instantaneous Stokes number for (a)  $Stk_{ref} = 0.05$ ; (b)  $Stk_{ref} = 0.2$ ; (c)  $Stk_{ref} = 0.4$ ; (d)  $Stk_{ref} = 0.8$  and (e)  $Stk_{ref} = 1.35$ . (For interpretation of the references to colour in this figure caption, the reader is referred to the web version of this paper.)

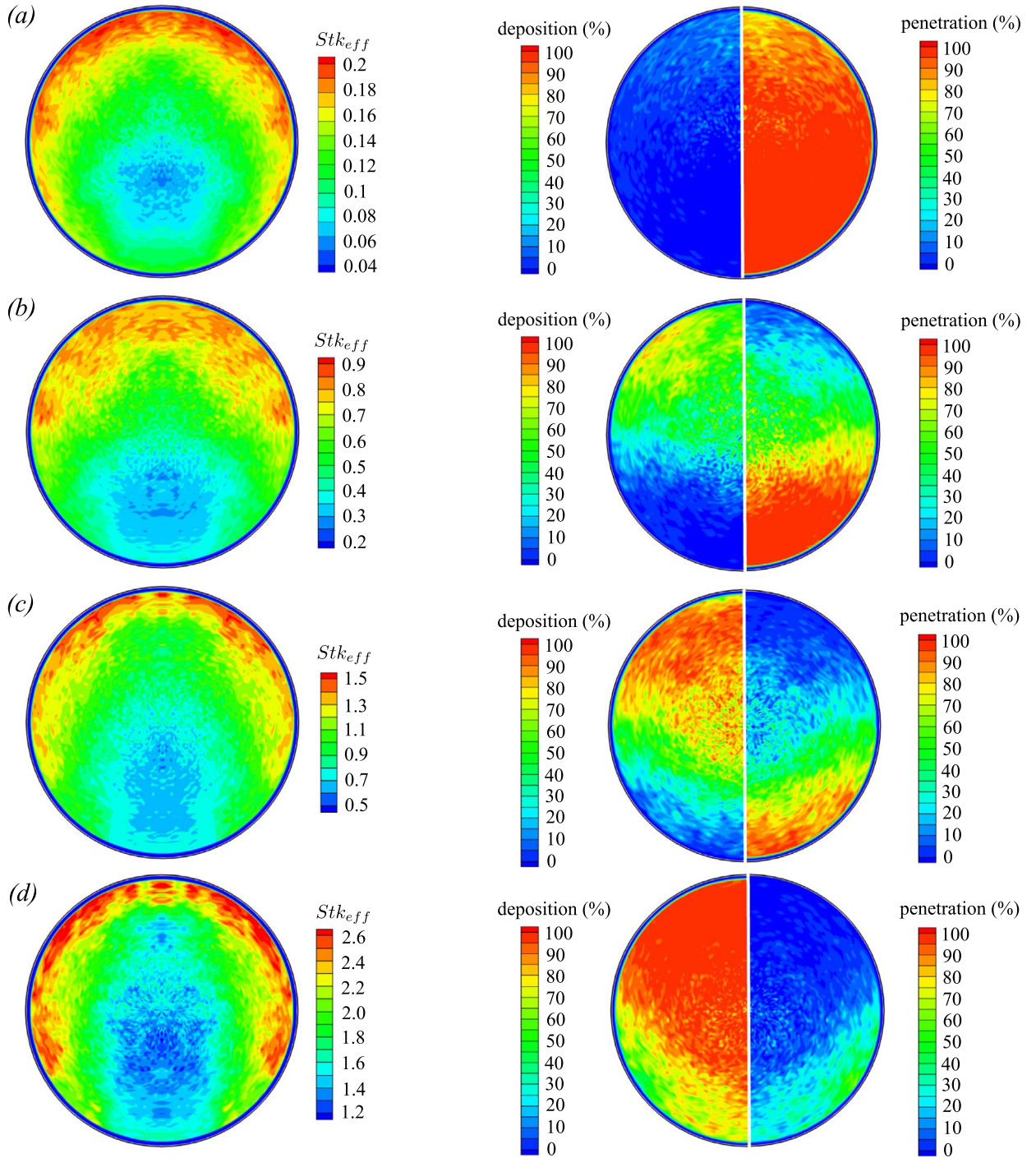


**Fig. 15.** Turbulent flow in curved pipe at  $Re_D=10,000$ : (a)  $Stk_{ref} = 0.05$ ; (b)  $Stk_{ref} = 0.2$ ; (c)  $Stk_{ref} = 0.4$ ; and (d)  $Stk_{ref} = 0.8$ . On the left: particles at inlet coloured by effective Stokes number; middle: deposition percentage based on release location; and right: penetration percentage based on release location. (For interpretation of the references to colour in this figure caption, the reader is referred to the web version of this paper.)

The probability density functions of  $Stk_{eff}$  for the four particle sizes are shown in Fig. 16. The separate probability distributions for particles that deposit and particles that do not deposit are also shown in red and blue, respectively. In all cases, the mean effective Stokes number is significantly higher than the reference value. As particle size increases, the spread in  $Stk_{eff}$  increases but the difference between the mean effective Stokes number for particles that deposit,  $Stk_{eff}^d$  and particles that remain undeposited,  $Stk_{eff}^f$ , decreases. Generally, a much larger spread in  $Stk_{eff}$  is observed across all particle sizes compared to the laminar case, since particles experience a wider range of flow timescales. Use of the instantaneous Stokes number based on the local properties of the flow field

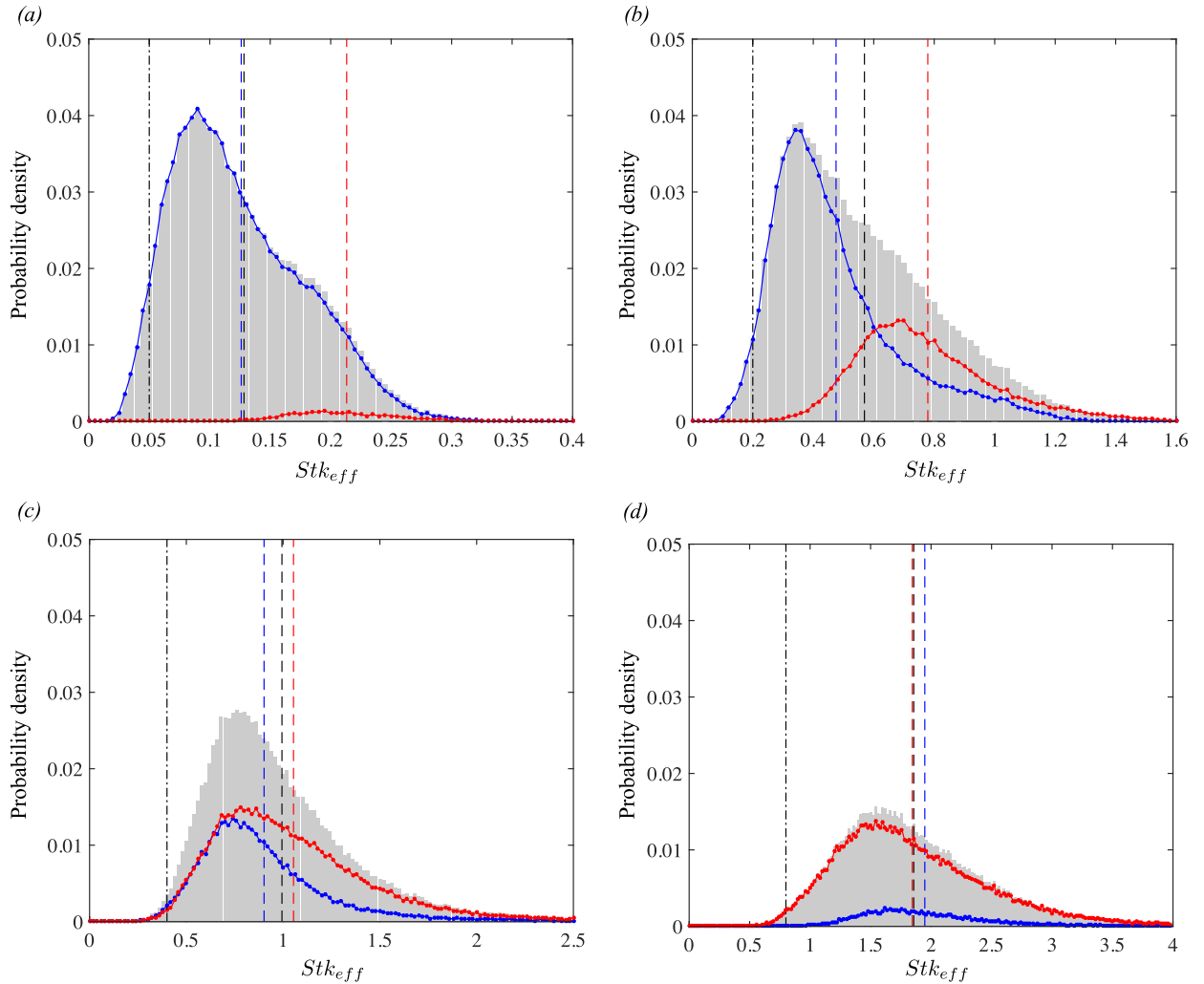


**Fig. 16.** Turbulent flow in curved pipe at  $Re_D=10,000$ : Pdf of effective Stokes number for (a)  $Stk_{ref} = 0.05$ ; (b)  $Stk_{ref} = 0.2$ ; (c)  $Stk_{ref} = 0.4$ ; and (d)  $Stk_{ref} = 0.8$ . ■ All particles; — particles not deposited; — deposited particles; lines as in Fig. 8.

allows us to extract these differences between the laminar and turbulent regimes, which are not taken into account in the reference Stokes number.

The deposition efficiencies versus  $Stk_{eff}$  for each particle size are shown in Fig. 17. Significant differences with the laminar case are observed in the intermediate Stokes number regime ( $0.3 < Stk_{ref} < 1.0$ ). For small particle sizes ( $Stk_{ref} < 0.3$ ), deposition versus  $Stk_{eff}$  follows the typical S-curve, which was also observed in the laminar case. For large particle sizes ( $Stk_{ref} > 1.0$ ), deposition plateaus as the effective Stokes numbers are high and all particles deposit via impaction in this regime. In the intermediate range ( $0.3 < Stk_{ref} < 1.0$ ), both impaction and turbulent dispersion contribute appreciably to deposition. The deposition efficiency versus  $Stk_{eff}$  in this regime follows a flat ‘U’ curve as the effect of dispersion diminishes with increasing  $Stk_{eff}$ .

### 3.2. Extrathoracic airways

Here we consider the flow and particle deposition in an idealized geometry of the extrathoracic airways (ETA). The adopted geometry is based on the model developed at the Aerosol Research Laboratory of Alberta (Stapleton, Guentsch, Hoskinson, & Finlay, 2000). It is representative of an average adult ETA with inhalation through a circular mouthpiece. Although it is a simplified model, it possesses all the basic anatomical features of realistic extrathoracic airways, and has been used in both *in vitro* (Grgic, Finlay, & Heenan, 2004; Heenan et al., 2003; Shinneeb & Pollard, 2012; Zhou, Sun, & Cheng, 2011) and numerical studies (Ball et al., 2008; Debhi, 2011; Matida et al., 2004).

A flow rate of  $Q=51.5$  L/min was assumed, which corresponds to a Reynolds number of  $Re_{inlet}=\rho_f U_{inlet} D_{inlet}/\mu_f = 3784$ , based on the inlet diameter and inlet velocity. The grid consisted of  $513 \times 257 \times 385$  points in the streamwise  $\xi$ , cross-stream  $\eta$ , and spanwise  $z$  direction, respectively. The grid spacing was  $0.015 < \Delta\xi < 0.05$  (near the outflow),  $0.003 < \Delta\eta < 0.01$  and  $\Delta z = 0.0064$ . This

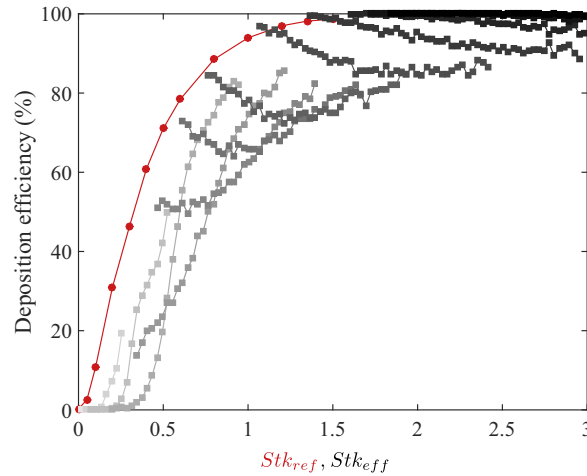


**Fig. 17.** Turbulent flow in curved pipe at  $Re_D=10,000$ : Deposition efficiency versus Stokes number.  $\bullet$   $Stk_{ref}$ ;  $\blacksquare$   $Stk_{eff}$  curves for each particle size, in ascending order. (Particle sizes are listed in Table 1.).

corresponds to  $3.86 < \Delta\xi^+ < 12.87$  (near the outflow),  $0.76 < \Delta\eta^+ < 2.60$  and  $\Delta z^+ = 1.64$ , based on the friction velocity at the inlet pipe. A simulation with double the number of grid points was also performed, but differences in the flow field and particle statistics were negligible. The grid and ETA geometry are shown in Fig. 18. A steady laminar inflow was prescribed, although the flow quickly transitions to turbulence towards the back of the oral cavity. Convective outflow conditions were applied at the exit plane.

Particles with diameters ranging from  $d_p = 2 \mu\text{m}$  to  $22 \mu\text{m}$  were released at uniformly distributed random locations over the inflow plane and tracked dynamically. The density ratio was set to  $\rho_p/\rho_f = 766$ , which corresponds to di-ethylhexyl sebacate (DEHS) particles in air at room temperature. The particles were released into the flow at regular intervals,  $\Delta t_{release} \sim 0.075 D_{inlet}/U_{inlet}$ , during a period of 4.95 time units, and advected for an additional four flow-through times. Approximately  $10^5$  particles were tracked for each size.

Contours of the mean velocity magnitude and turbulent kinetic energy per unit mass in the idealized ETA geometry are shown in Fig. 19. Due to the airway curvature, the flow entering the mouth shifts towards the outer wall, with recirculation regions forming above and below the incoming jet (Fig. 19a and b). The flow accelerates at the back of the mouth as the cross-sectional area decreases, developing a pharyngeal jet which impinges onto the epiglottis. Further downstream, a pronounced separated shear layer develops due to the bend in the airway, and impinges on the anterior wall of the trachea. A recirculation region can also be observed near the outer wall of the trachea, under the ‘sharp step’ in the larynx. The maximum kinetic energy occurs in the pharynx near the jet, and in the trachea near the location of the separated shear layer (Fig. 19c). The flow features in the idealized model are similar to those observed in realistic extrathoracic airway geometries (Heenan et al., 2004; Jayaraju et al., 2007; Nicolaou & Zaki, 2013).

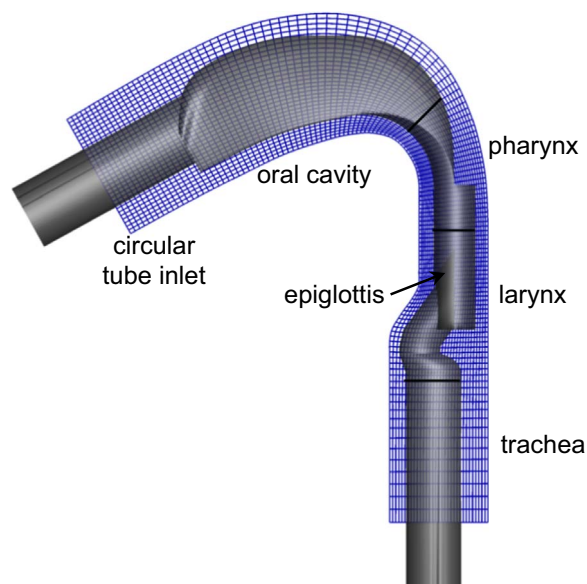


**Fig. 18.** The idealized geometry and curvilinear grid adopted for the extrathoracic airways. Every fourth grid line in  $\xi$  and eighth grid line in  $\eta$  has been plotted.

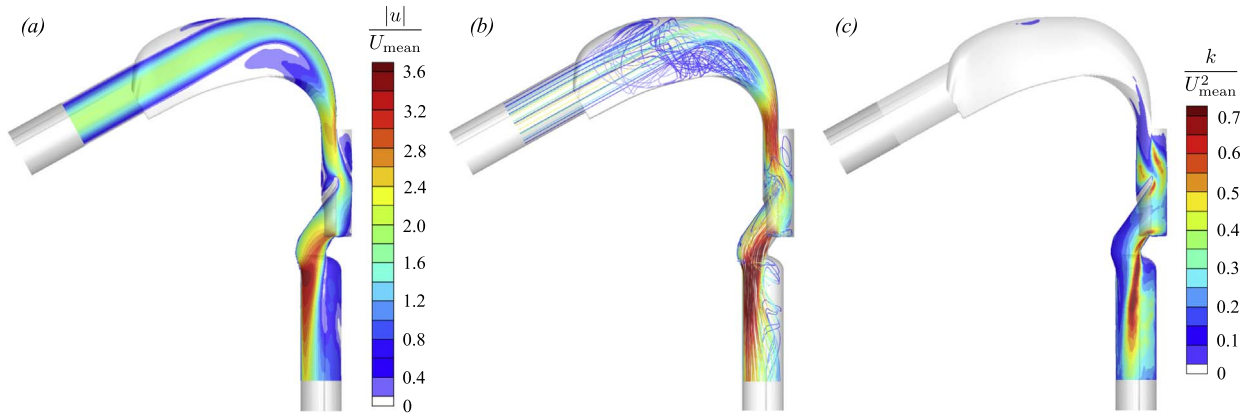


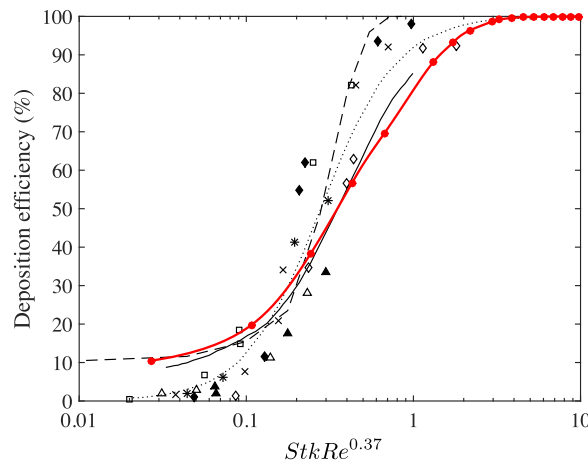
**Fig. 19.** (a) Contours of mean velocity magnitude; (b) streamlines of the time-averaged flow coloured by mean velocity and (c) contours of turbulent kinetic energy per unit mass in central sagittal plane of idealized ETA geometry. (For interpretation of the references to colour in this figure caption, the reader is referred to the web version of this paper.)

The deposition efficiency versus Stokes number with Reynolds number correction,  $StkRe^{0.37}$ , is shown in Fig. 20 alongside *in vitro* and numerical results from the literature. Note that the Reynolds number used in this plot is  $Re_{mean} = \rho_f U_{mean} D_{mean} / \mu_f$ , which is based on the mean equivalent diameter and corresponding mean velocity. In the current simulation,  $Re_{mean} = 3421$ . The current study and that by Debhi (2011) were performed in the same idealized geometry. In their study a slightly smaller mouthpiece of diameter 17 mm was employed, in comparison to ours ( $D_{inlet} = 19$  mm). Nonetheless, there is good agreement between the two studies. Significant scatter is observed, however, across the *in vitro* data and other numerical results. This scatter can be attributed primarily to the geometric variability across subjects' extrathoracic airways. Geometric variation has a significant effect on the flow field, and can lead to qualitatively different flow features in different airways. Therefore, even with the same particle Stokes number and mean flow Reynolds number, deposition efficiencies will vary across geometries (Nicolaou & Zaki, 2013).

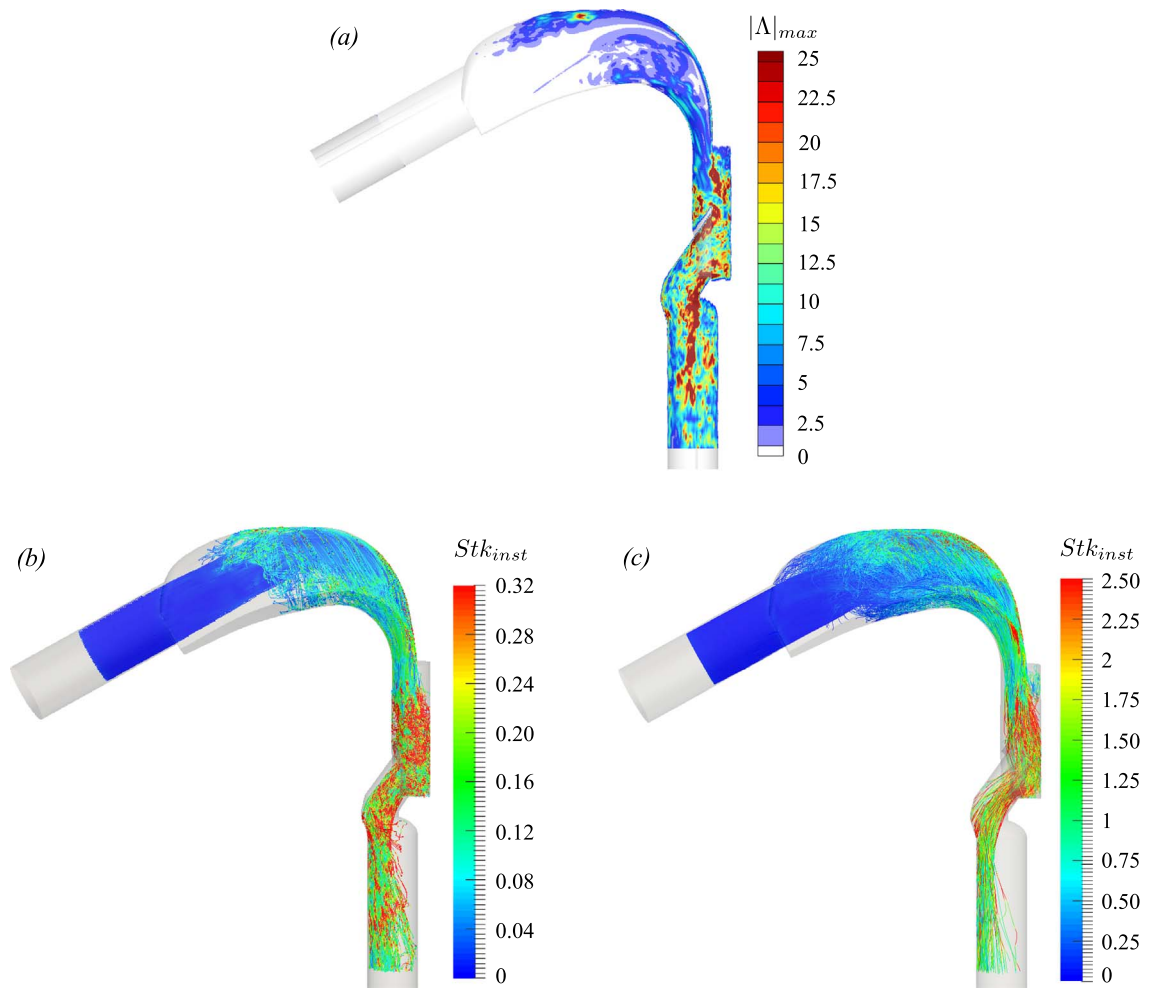
The particle trajectories in the idealized geometry, coloured by the instantaneous Stokes number, are shown in Fig. 21 for two particle sizes. A snapshot showing contours of  $|A|_{max}$  in the central sagittal plane is also displayed in Fig. 21a. It is evident that the initially laminar flow rapidly becomes turbulent inside the oral cavity. The early section resembles the laminar bent pipe. As flow transitions downstream, the particle Stokes numbers increase. The highest Stokes numbers are experienced in the larynx and trachea, where the velocity gradients increase significantly. The trajectories of the small particles are influenced by the velocity fluctuations (Fig. 21b), whereas the larger particles display a more ballistic behaviour, as can be seen in the larynx and trachea in Fig. 21c. A more pronounced shift towards the front wall of the trachea is also observed for the larger size, as the particles are unable to respond to the sudden change in flow direction due to their high inertia.

Fig. 22 shows the deposition patterns for the two particle sizes. The deposited particles are shown coloured by their instantaneous Stokes number at the time of deposition. For both particle sizes, the larynx is a main region of deposition. This corresponds to the region of highest  $\Lambda_{max}$ , as seen in Fig. 21a.

For the small particles, high deposition is also observed in the trachea, with particles uniformly deposited in this area. The large particles, on the other hand, exhibit a pronounced hotspot on the front wall of the trachea and negligible deposition along the back



**Fig. 20.** Deposition efficiency versus  $StkRe^{0.37}$  for idealized ETA geometry. Current simulation shown in red. Numerical results at  $Q=60$  L/min: --- (Jayaraju et al., 2007) and — (Debhi, 2011). Symbols are *in vitro* data across a number of geometries (Grgic, Finlay, Burnell, et al., 2004); ... *in vitro* data fit. (For interpretation of the references to colour in this figure caption, the reader is referred to the web version of this paper.)



**Fig. 21.** (a) Snapshot of  $|\Delta|_{max}$  and particle trajectories coloured by their instantaneous Stokes number for (b)  $d_p = 6 \mu m$  ( $Stk_{ref} = 0.012$ ) and (c)  $d_p = 18 \mu m$  ( $Stk_{ref} = 0.107$ ). (For interpretation of the references to colour in this figure caption, the reader is referred to the web version of this paper.)

wall. Light particles enter the recirculation region behind the separated shear layer and eventually deposit on the back wall of the trachea whereas the large particles have a higher inertia and so deposit on the front wall, where the separated shear layer impinges.

At the larger particle size, a significant increase in deposition is observed, particularly along the upper wall of the mouth and upper pharynx (Figs. 22d–f). Larger particles experience higher  $Stk_{inst}$  in this area, which causes them to deposit via impaction on the outer wall. Deposition can also be observed on the lower wall of the inlet tube and mouth. These deposited particles, however, exhibit relatively low instantaneous Stokes numbers. Deposition in this region is via sedimentation rather than impaction, as low-speed particles travelling near the wall have time to settle onto the bottom wall due to gravity.

The effective Stokes number of the particles is visualized at their initial location in Fig. 23 for four different particle sizes. Contours of the deposition fractions are displayed in the middle column, and the insertion locations which lead to deposition are visualized at right. As observed in the bent pipe, a significant spread in effective Stokes number exists across all particle sizes. For a given size, particles experience very different values of  $Stk_{eff}$  depending on their initial release position. The smaller particles (Figs. 23a and b) experience generally low Stokes numbers and so travel further downstream before depositing. Deposition for these two particle sizes occurs primarily in the larynx and trachea. For the  $12 \mu m$  particles (Fig. 23c), higher levels of deposition are recorded in the mouth and pharynx as particles begin to deposit earlier on, due to their increased inertia. As particle size increases even further, the majority of deposition occurs in the mouth (Fig. 23d). Here, the relatively low values of  $Stk_{eff}$  observed at the centre of the inlet are due to the particles depositing before reaching the regions of high velocity gradients and, as a result, high instantaneous Stokes numbers (i.e. the larynx and trachea).

Fig. 24 shows the probability distributions of  $Stk_{eff}$  for the four particle sizes. The separate probability distributions for particles that have deposited, particles that remain in the flow domain and particles that have exited the trachea are also shown in red, green and cyan, respectively. The blue line represents the probability density of all particles that have not deposited, i.e. particles that have exited the trachea as well as those remaining in the flow. In all cases, the mean effective Stokes number is considerably higher than the reference Stokes number based on the bulk velocity and mean diameter of the ETA geometry. As expected, for small particle

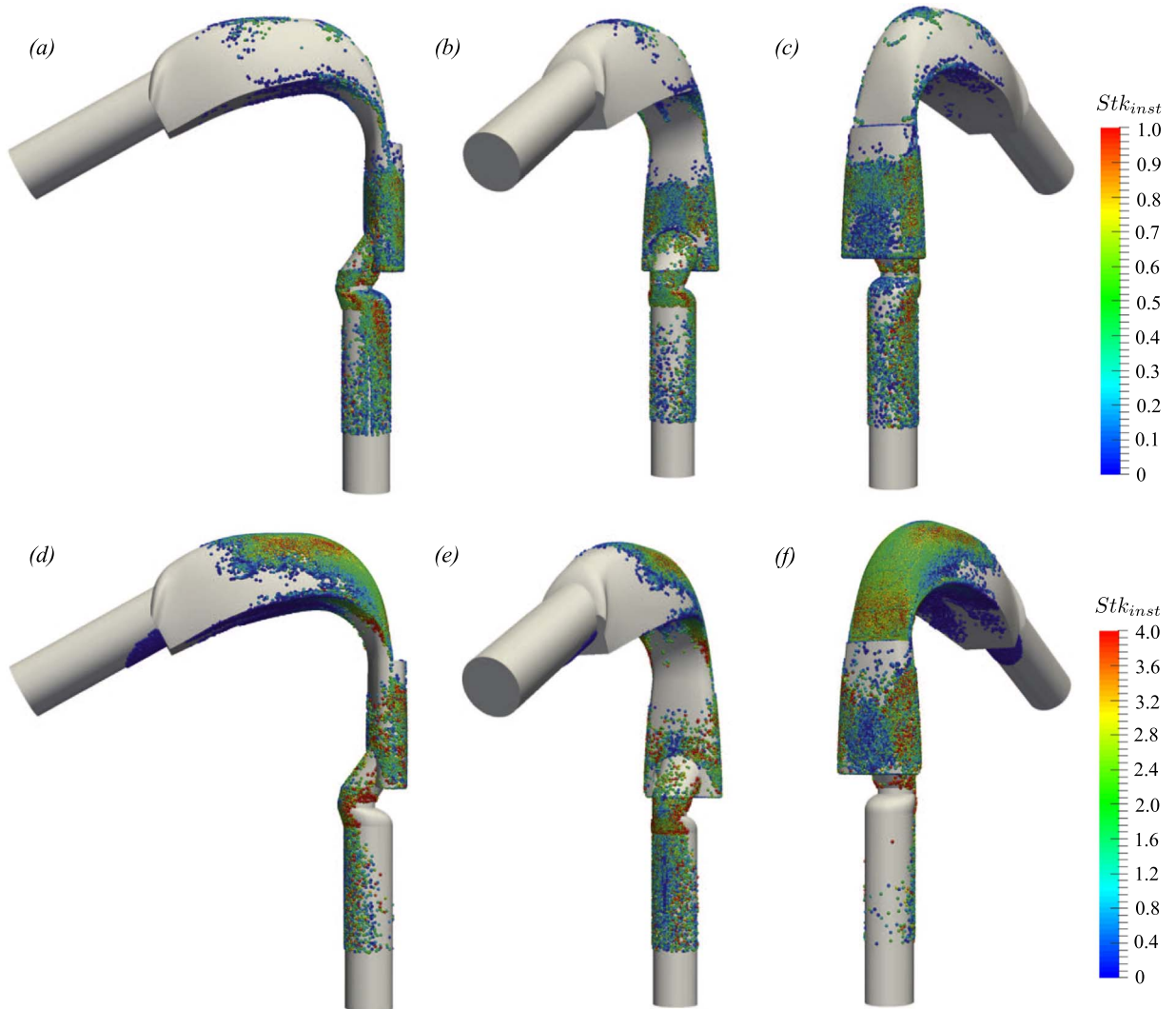


**Fig. 22.** Deposition patterns in the extrathoracic airways. Particles coloured by their instantaneous Stokes number for (a–c)  $d_p = 6 \mu\text{m}$  ( $Stk_{ref} = 0.012$ ) and (d–f)  $d_p = 18 \mu\text{m}$  ( $Stk_{ref} = 0.107$ ). (For interpretation of the references to colour in this figure caption, the reader is referred to the web version of this paper.)

sizes, the majority of particles exit the trachea and only a small percentage deposit (Fig. 24a and b). As particle size increases, this trend reverses, with a larger proportion of the particles depositing and a small amount exiting the airways (Fig. 24c and d). Across all sizes, the particles that remain suspended in the flow domain are those with low effective Stokes numbers. These are low-speed particles travelling near the airway walls. At  $d_p = 18 \mu\text{m}$ , a small peak in deposition is observed at very low  $Stk_{eff}$  (Fig. 24d). This peak corresponds to the particles depositing on the inlet tube and bottom wall of the mouth via sedimentation (see Fig. 22d–f).

The instantaneous and effective Stokes numbers provide a more detailed view of the deposition trends in the extrathoracic airways, which is informative in the optimization of inhaled drug delivery. The results presented in this section demonstrate that it is not sufficient to simply choose a particular reference Stokes number, or particle size, in order to minimize extrathoracic losses. Deposition varies significantly depending on the release location of the particles, and the deposition/penetration zones differ across particle sizes. Additionally, intersubject variation, which is known to have a significant effect on the flow characteristics, is also expected to have a considerable impact on optimum release locations.

#### 4. Summary

Aerosol deposition in the airways is typically described as a function of the reference Stokes number, based on a global length and velocity scale for the flow field. Most commonly, the mean flow velocity and mean airway diameter are used. This reference Stokes number does not, however, capture the influence of flow history or geometric variability. The flow time scales experienced by particles as they are advected through the flow are expected to deviate significantly from the reference value, and geometric variability can lead to qualitatively different flow features and as such alter particle deposition appreciably. In order to characterize

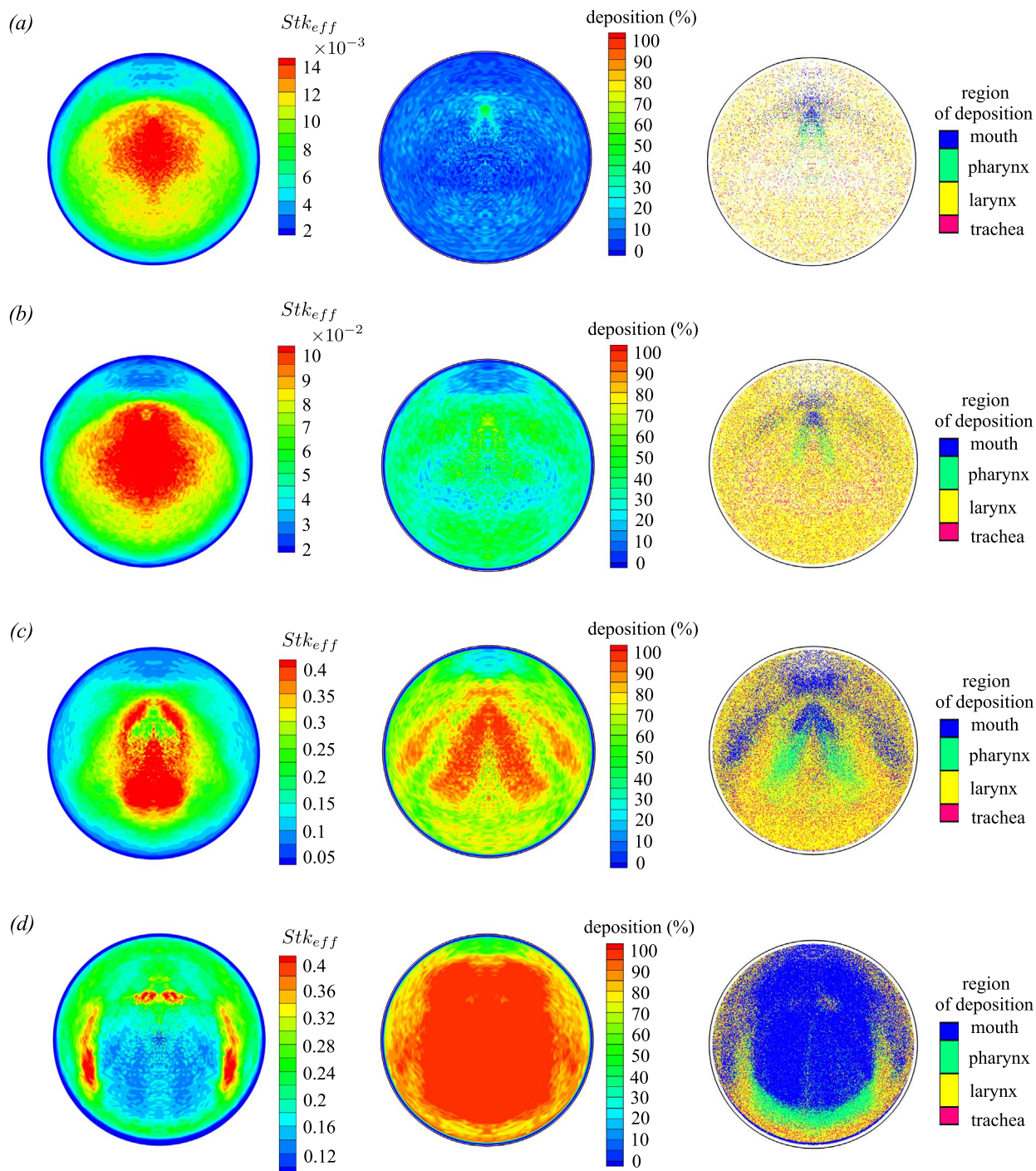


**Fig. 23.** Extrathoracic airways: (a)  $d_p = 2 \mu\text{m}$  ( $Stk_{ref} = 0.0013$ ); (b)  $d_p = 6 \mu\text{m}$  ( $Stk_{ref} = 0.012$ ); (c)  $d_p = 12 \mu\text{m}$  ( $Stk_{ref} = 0.0647$ ); and (d)  $d_p = 18 \mu\text{m}$  ( $Stk_{ref} = 0.107$ ). On the left: particles at inlet characterized by effective Stokes number; middle: deposition percentage based on release location; and right: region of deposition based on release location.

particle transport and deposition, the use of an instantaneous Stokes number was proposed, based on the local properties of the flow field. Time-averaging this instantaneous value yields the effective Stokes number of the particle which is better representative of its trajectory.

Particle dynamics were examined in three different flow configurations: (i) laminar and (ii) turbulent flows in bent pipes and (iii) turbulent flow in the extrathoracic airways. The bent pipe serves as a canonical test case for the extrathoracic region, which enables us to examine the effect of the flow history on the particles without the complexity of the geometry. The effective Stokes number was

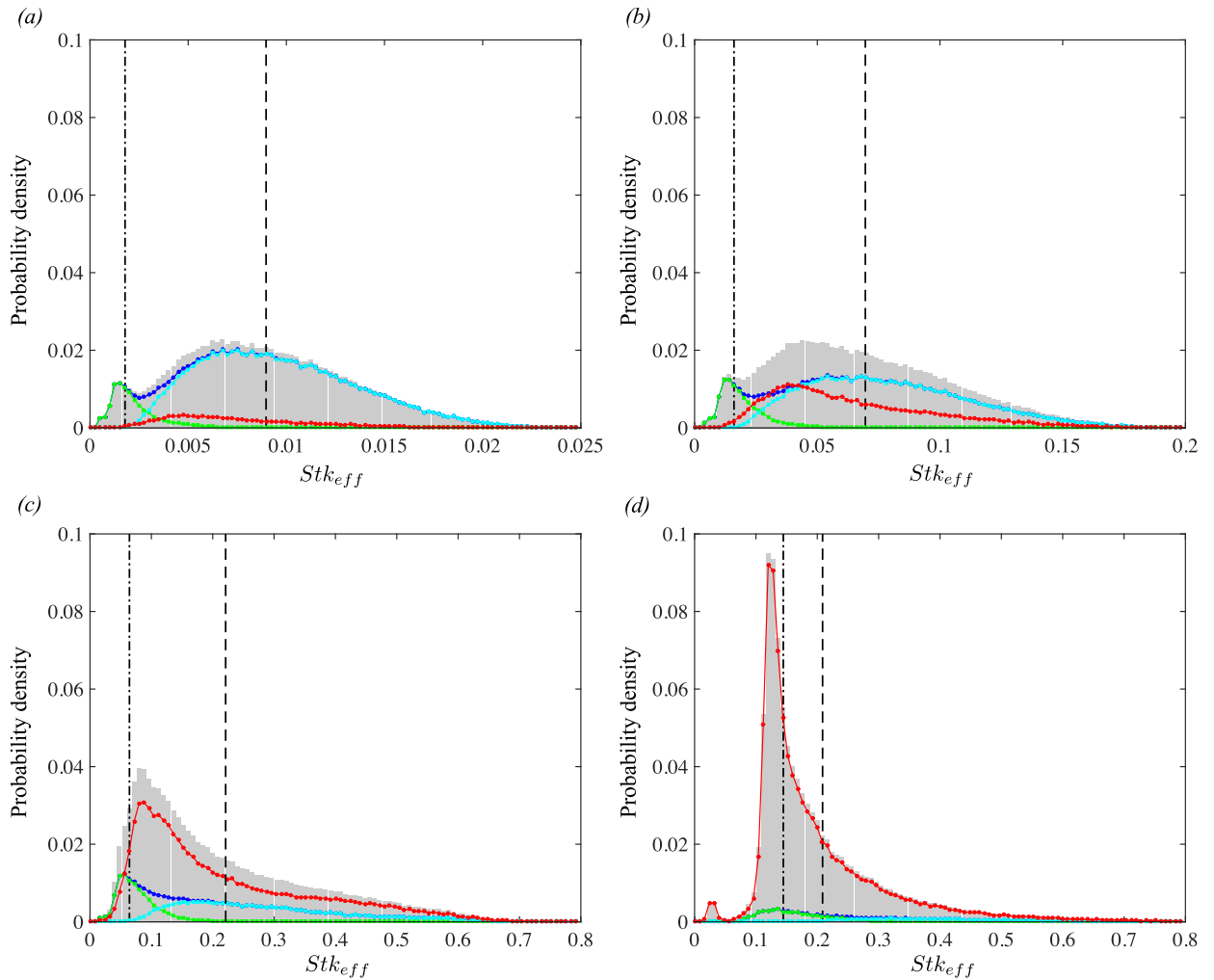


**Fig. 24.** Extrathoracic airways: probability density function of effective Stokes number for (a)  $d_p = 2 \mu\text{m}$ ; (b)  $d_p = 6 \mu\text{m}$ ; (c)  $d_p = 12 \mu\text{m}$ ; and (d)  $d_p = 18 \mu\text{m}$ . ■ All particles; — deposited particles; — particles not deposited; — particles still in the flow domain; — particles that have exited trachea. --- reference Stokes number,  $Stk_{ref}$ ; - - - mean effective Stokes number,  $\overline{Stk_{eff}}$ .

shown to vary significantly between the laminar and turbulent flow cases: A particle with the same size and same release location experiences significantly different local Stokes numbers as it is advected through the flow in the two configurations. Therefore, the penetration/deposition regions also differ appreciably between the two flows. In the laminar case, these regions were sharply defined and a clear correlation between effective Stokes number and deposition was observed. In the turbulent case, these regions were less distinct as a result of turbulence mixing. In both cases, the effective Stokes number was shown to deviate considerably from the reference value. Significant variance in the distribution of the effective Stokes number,  $Stk_{eff}$ , was also observed, with  $Stk_{eff}$  depending on the release location of the particle.

The idealized extrathoracic airway model adopted in the present study is representative of an average adult upper airway geometry. A laminar inflow was prescribed with a flow rate of 51.5 L/min, and the flow rapidly became turbulent inside the oral cavity. The larynx, where local Stokes numbers were highest, was found to be a main region of deposition across all particle sizes. For increasing particle size, higher levels of deposition were observed in the mouth and pharynx as particles experienced higher Stokes numbers earlier on, thereby depositing via impaction. Across all particle sizes examined, the mean effective Stokes number was shown to be considerably higher than the reference value. Similar to the bent pipe, a significant spread in effective Stokes number was observed.

The cases presented herein have adopted steady inflow (constant flow rate) and idealized geometries. The effective Stokes number will vary for different airway geometries and flow conditions. Nevertheless, the results demonstrate the value of this parameter in characterizing deposition. The use of the effective Stokes number in patient-specific geometries, and for inhalation characteristics, can provide a richer representation of the effect of geometric variation and of the flow on the particle dynamics. By encapsulating the influence of the flow history, the effective Stokes number provides a better account of the particle trajectories within the airways, for both steady and unsteady inhalation. This parameter also demonstrates how the combined choice of particle

size and release location has a significant effect on deposition. As such, it can assist in the assessment of inhaled drug delivery and it can guide the choice of particle release locations, particle size distribution and flow conditions for optimum delivery to the lungs.

## Acknowledgements

L. Nicolaou would like to acknowledge the financial support provided by the Imperial College Research Fellowship.

## References

- Ball, C., Uddin, M., & Pollard, A. (2008). Mean flow structures inside the human upper airway. *Flow, Turbulence and Combustion*, 81, 155–188.
- Breuer, H. T., Baytekin, M., & Matida, E. A. (2006). Prediction of aerosol deposition in 90° bends using LES and an efficient Lagrangian tracking method. *Journal of Aerosol Science*, 37, 1407–1428.
- Cheng, Y. S., & Wang, C. S. (1981). Motion of particles in bends of circular pipes. *Atmospheric Environment*, 15, 301–306.
- Cheng, Y. S., Zhou, Y., & Chen, B. T. (1999). Particle deposition in a cast of human oral airways. *Aerosol Science and Technology*, 31, 286–300.
- Debhi, A. (2011). Prediction of extrathoracic aerosol deposition using RANS-random walk and LES approaches. *Aerosol Science and Technology*, 45, 555–569.
- Eggels, J. G., Unger, F., Weiss, M. H., Westerweel, J., Adrian, R. J., Friedrich, R. et al. (1994). Fully developed turbulent pipe flow: A comparison between direct numerical simulation and experiment. *Journal of Fluid Mechanics*, 268, 175–209.
- Elghobashi, S. (1994). On predicting particle-laden turbulent flows. *Applied Scientific Research*, 52, 309–329.
- Grgic, B., Finlay, W., Burnell, P., & Heenan, A. (2004). In vitro intersubject and intrasubject deposition measurements in realistic mouth–throat geometries. *Journal of Aerosol Science*, 35, 1025–1040.
- Grgic, B., Finlay, W., & Heenan, A. (2004). Regional aerosol deposition and flow measurements in an idealized mouth and throat. *Journal of Aerosol Science*, 35, 21–32.
- Heenan, A., Finlay, W., Grgic, B., Pollard, A., & Burnell, P. (2004). An investigation of the relationship between the flow field and regional deposition in realistic extrathoracic airways. *Journal of Aerosol Science*, 35, 1013–1023.
- Heenan, A., Matida, E., Pollard, A., & Finlay, W. (2003). Experimental measurements and computational modeling of the flow field in an idealized human oropharynx. *Experiments in Fluids*, 35, 70–84.
- Jayaraju, S., Brouns, C., Lacor, C., Belkassam, B., & Verbanck, S. (2008). Large eddy and detached eddy simulations of fluid flow and particle deposition in a human mouth–throat. *Journal of Aerosol Science*, 39, 862–875.
- Jayaraju, S. T., Brouns, M., Verbanck, S., & Lacor, C. (2007). Fluid flow and particle deposition analysis in a realistic extrathoracic airway model using unstructured grids. *Journal of Aerosol Science*, 38, 494–508.
- Jelly, T., Jung, S., & Zaki, T. (2014). Turbulence and skin friction modification in channel flow with streamwise-aligned superhydrophobic surface texture. *Physics of Fluids*, 26, 095102.
- Jung, S. Y., & Zaki, T. (2015). The effect of a low-viscosity near-wall film on bypass transition in boundary layers. *Journal of Fluid Mechanics*, 772, 330–360.
- Kim, J., Moin, P., & Moser, R. (1987). Turbulence statistics in fully developed channel flow at low Reynolds number. *Journal of Fluid Mechanics*, 177, 133–166.
- Kleinstreuer, C., & Zhang, Z. (2003). Laminar-to-turbulent fluid–particle flows in a human airway model. *International Journal of Multiphase Flow*, 29, 271–289.
- Lee, J., Jung, S. Y., Sung, H. J., & Zaki, T. A. (2013). Effect of wall heating on turbulent boundary layers with temperature-dependent viscosity. *Journal of Fluid Mechanics*, 726, 196–225.
- Li, Z., Kleinstreuer, C., & Zhang, Z. (2007). Particle deposition in the human tracheobronchial airways due to transient inspiratory flow patterns. *Journal of Aerosol Science*, 38, 625–644.
- Lin, C.-L., Tawhai, M. H., McLennan, G., & Hoffman, E. A. (2007). Characteristics of the turbulent laryngeal jet and its effect on airflow in the human intra-thoracic airways. *Respiratory Physiology & Neurobiology*, 157, 295–309.
- Matida, E., Finlay, W., Lange, C., & Grgic, B. (2004). Improved numerical simulation of aerosol deposition in an idealized mouth–throat. *Journal of Aerosol Science*, 35, 1–19.
- Nicolaou, L., Jung, S., & Zaki, T. A. (2015). A robust direct-forcing immersed boundary method with enhanced stability for moving body problems in curvilinear coordinates. *Computers & Fluids*, 119, 101–114.
- Nicolaou, L., & Zaki, T. A. (2013). Direct numerical simulations of flow in realistic mouth–throat geometries. *Journal of Aerosol Science*, 57, 71–87.
- Pilou, M., Tsangaris, S., Neofytou, P., Housiadas, C., & Drossinos, Y. (2011). Inertial particle deposition in a 90° laminar flow bend: An Eulerian fluid particle approach. *Aerosol Science and Technology*, 45, 1376–1387.
- Pui, D. Y. H., Romay-Novas, F., & Liu, B. Y. H. (1987). Experimental study of particle deposition in bends of circular cross section. *Aerosol Science and Technology*, 7, 301–315.
- Rosenfeld, M., Kwak, D., & Vinokur, M. (1991). A fractional step solution method for the unsteady incompressible Navier–Stokes equation in generalized coordinate systems. *Journal of Computational Physics*, 94, 102–137.
- Schiller, L., & Naumann, A. (1933). A drag coefficient correlation. *VDI Zeitschrift*, 77, 318–320.
- Shinneeb, A. M., & Pollard, A. (2012). Investigation of the flow physics in the human pharynx/larynx region. *Experiments in Fluids*, 53, 989–1003.
- Shirayama, S. (1993). Processing of computed vector fields for visualization. *Journal of Computational Physics*, 30–41.
- Stahlhofen, W., Gebhart, J., & Heyder, J. (1981). Biological variability of regional deposition of aerosol particles in the human respiratory tract. *American Industrial Hygiene Association Journal*, 42, 348–352.
- Stapleton, K. W., Guentsch, E., Hoskinson, M. K., & Finlay, W. H. (2000). On the suitability of  $k$ - $\epsilon$  turbulence modeling for aerosol deposition in the mouth and throat: A comparison with experiment. *Journal of Aerosol Science*, 31, 739–749.
- Trujillo, M. F., & Parkhill, A. E. (2011). A local Lagrangian analysis of passive particle advection in a gas flow field. *International Journal of Multiphase Flow*, 37, 1201–1208.
- Tsai, C. J., & Pui, D. Y. H. (1990). Numerical study of particle deposition in bends of a circular cross-section – Laminar flow regime. *Aerosol Science and Technology*, 12, 813–831.
- Zaki, T. A. (2013). From streaks to spots and on to turbulence: exploring the dynamics of boundary layer transition. *Flow, Turbulence and Combustion*, 91, 451–473.
- Zhang, Z., Kleinstreuer, C., & Kim, C. S. (2002). Micro-particle transport and deposition in a human airway model. *Journal of Aerosol Science*, 33, 1635–1652.
- Zhou, Y., Sun, J., & Cheng, Y. (2011). Comparison of deposition in the USP and physical mouth–throat models with solid and liquid particles. *Journal of Aerosol Medicine and Pulmonary Drug Delivery*, 24, 277–284.